H.E. Coules, S. O. Nneji, J. A. James, S. Kabra, J. N. Hu, Y. Wang

Full-tensor measurement of multiaxial creep stress relaxation in Type 316H stainless steel

Full-tensor measurement of multiaxial creep stress relaxation in Type 316H stainless steel

H.E. Coules, S. O. Nneji, J. A. James, S. Kabra, J. N. Hu, Y. Wang

Full-tensor measurement of multiaxial creep stress relaxation in Type 316H stainless steel

H.E. Coules[1], S. O. Nneji[2,3], J. A. James[2], S. Kabra[3], J. N. Hu[4,5], Y. Wang[6]

[1] Department of Mechanical Engineering, University of Bristol, Bristol, BS8 1TR, UK

[2] Materials Engineering, The Open University, Walton Hall, Milton Keynes, MK7 6AA, UK

[3] ISIS Facility, STFC Rutherford Appleton Laboratory, Didcot, Oxfordshire, OX11 0QX, UK

[4] Department of Engineering Science, University of Oxford, Oxford, OX1 3PJ, UK

[5] Sente Software Ltd., Surrey Research Park, Guildford, Surrey, GU2 7YG, UK

[6] United Kingdom Atomic Energy Authority, Culham Centre for Fusion Energy, Abingdon, Oxfordshire, OX14 3DB, UK

Graphical abstract
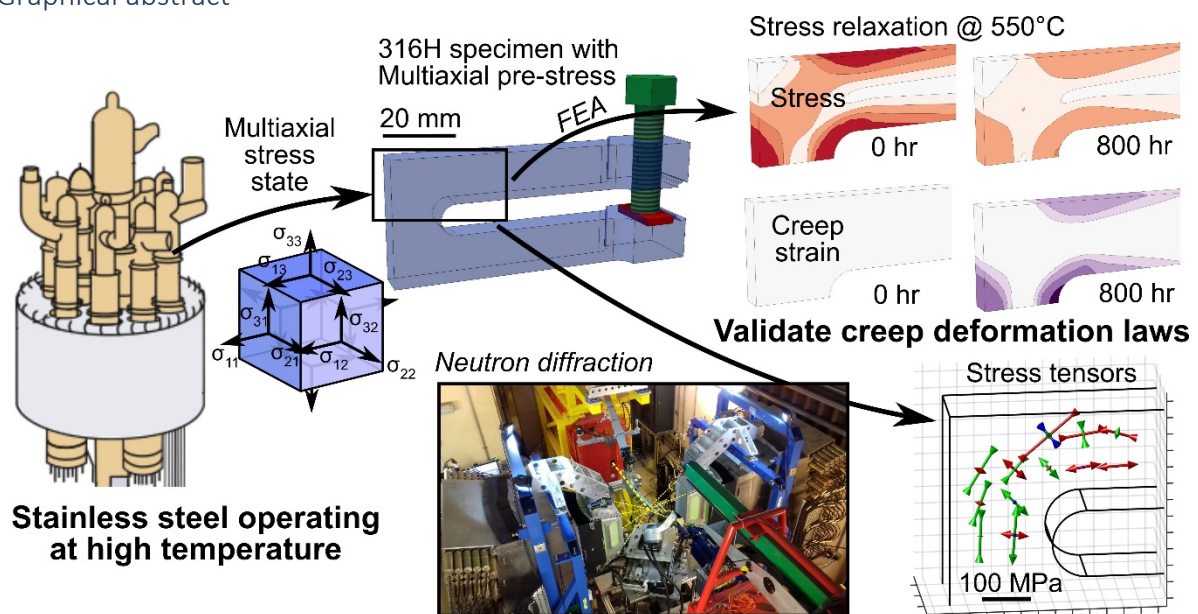
Abstract

Mechanical constitutive models of metals undergoing deformation in three dimensions can be challenging to validate without loss of generality. For example, creep-induced stress relaxation in stainless steels has previously been studied using axisymmetric notched-bar tests which control the triaxiality of the initial stress state. However, such experiments only provide partial insight into the creep process that causes the specimen's stress state to vary spatially and over time. We have used time-of-flight neutron diffraction to track the complete stress tensor at 12 interior locations within specimens of Type 316H stainless steel containing a complex stress field as it relaxes due to creep. Using such data, it is possible to check the accuracy of creep laws (such as the widely-used RCC-MR model) in the general multiaxial case. Over-determination of the elastic strain tensor using measurements in multiple directions also helps to reduce measurement uncertainty. Our results indicate that the RCC-MR primary/secondary creep law for Type 316H is conservative for cases involving a complex initial stress field.

Keywords

Stress relaxation; neutron diffraction; creep; stainless steel; multiaxiality; residual stress

Highlights

- Neutron diffraction enables measurement of complete stress tensors inside homogeneous stainless steel specimens subject to high-temperature stress relaxation.
- Material deformation processes which cause a non-proportional change in multiaxial stress can be studied.
- Comparison with finite element analysis confirms that a widely-used creep rate law is conservative for multiaxial stressing.
- Reduction in stress tensor uncertainty is achievable using over-determined neutron diffraction measurements.

1. Introduction

AISI/SAE Type 316H austenitic stainless steel is used extensively for nuclear power reactor internal components in UK Advanced Gas-cooled Reactors (AGRs). These CO_2-cooled reactors operate at coolant outlet temperatures of up to 640°C [1]. Typical service temperatures for Type 316H components are between 470°C and 650°C. Typical stresses are in the range 100-300 MPa and mostly thermal or residual in nature [2]. One life-limiting factor for AGRs is the condition of the steam generators, which in AGR designs are located inside the reactor's reinforced concrete pressure vessel. Some parts of the steam generators are vulnerable to creep; particularly the superheaters which experience the highest temperatures (up to around 620°C inlet gas temperature).

The creep damage and creep rupture properties of metals are strongly affected by stress multiaxiality. This has led to the development of specialised test methods to measure creep rupture under multiaxial stress [3–5]. Material models which include the effect of stress multiaxiality on creep damage are now in common use and have been included in the R5 structural integrity assessment procedure maintained by EDF Energy and others [6]. By contrast, the effect of multiaxial stress on creep deformation is less well understood. For isotropic materials, it is normally accepted that creep deformation rate models which use a scalar effective stress based on the second invariant of the stress deviator tensor (J_2) are accurate for multiaxial creep in the primary and secondary regimes [7], [8]. This is consistent with the physical assumptions that: a.) if the material is isotropic then the creep rate tensor ($\dot{\varepsilon}_{ij}^{cr}$) must be an isotropic function of the stress tensor (σ_{ij}) and b.) primary and secondary creep do not cause a bulk creep strain ($\dot{\varepsilon}_{ii}^{cr} = 0$) [9], [10].

For a few materials and conditions, the scalar effective stress approach to estimating the creep deformation rate in the primary and secondary regimes is more difficult to justify. The Type IV region of ferritic steel welds are one example [11]: inhomogeneous evolution of microstructure and stress can lead to a creep deformation rate which appears to have a dependence on the maximum principal stress [12]. Issues such as these have led to the development of generalised creep potentials [13]. Furthermore, in most metals the formation of micro-cavities and other forms of damage during tertiary creep can cause both bulk strain and material anisotropy. This creates a further source of error for conventional creep deformation laws. Physically-based approaches, such as the popular Cocks & Ashby model [14] and more recently the model proposed by Spindler [15], have proved useful for estimating damage at larger creep strains and hence for predicting the ductility of materials in multiaxial creep.

In structures where residual and/or thermal stresses cause the localisation of creep strain due to elastic follow-up, any errors in prediction of the creep deformation rate can be greatly magnified [16]. Furthermore, residual and thermal stresses can affect the local stress triaxiality. Therefore, accurate creep deformation rate models are particularly important in structures where thermal and residual

stresses occur. By accounting for the effects of multiaxial stress more accurately, it might be possible to provide more reliable predictions of primary and secondary creep strain accumulation in these complex structures. This would allow engineers to give better assessments of structural integrity for high temperature systems, aiding both design and life-extension efforts.

A major barrier to the development of generalised creep deformation models is the difficulty involved in experimentally observing multiaxial creep prior to the tertiary regime. For example, the evolution of the stress state inside a metal specimen undergoing multiaxial creep cannot be measured directly using conventional methods. For creep specimens containing non-uniform stress states, materials or temperature distributions, the total multiaxial strain on the surface can be measured using (for example) strain gauge rosettes or high-temperature Digital Image Correlation (DIC) [17], [18]. More frequently, easier-to-determine quantities such as overall extension and dilatational strain of a notched cylindrical specimen are measured and related to deformation rate models via Finite Element Analysis (FEA). Only relatively simple deformation rate models containing few material-dependent parameters can be confidently fitted using this limited experimental data.

In this work, we examine the feasibility of using neutron diffraction measurements to study multiaxial creep stress relaxation. An experiment in which relaxation of a multiaxial stress occurs would be more closely representative of real AGR conditions than conventional creep tests and neutron diffraction provides a means to probe complex stress fields. Specimens of Type 316H stainless steel containing a non-uniform residual stress were created. They were exposed to high temperature for different lengths of time and the resulting partially-relaxed stress states were studied in detail using neutron diffraction. By comparing the results to those from a set of FE models which used a creep deformation model with a single creep potential, we aimed to assess the suitability of such models for predicting multiaxial creep stress relaxation, and particularly the suitability of diffraction methods for investigating changing multiaxial stress states.

2. Method

2.1. Overview

Stress relaxation tests were performed using purpose-designed Double-Cantilever Beam (DCB) specimens of ex-service Type 316H austenitic stainless steel, shown in Figure 1. After manufacture, each specimen was pre-stressed by using a Nimonic 80A loading screw to open the mouth of the cantilevers to a predefined opening displacement to produce a residual stress field. The specimens were then heated to 550°C to allow stress relaxation to occur in the sample while the loading screw remained elastic. Each specimen was held at this temperature for a different length of time. After cooling, the residual stresses remaining in the specimens were measured using neutron diffraction. The results were compared with those of a FE model which simulated the stress relaxation process.

2.2. Material

The material used was taken from an ex-service AGR steam header of the well-studied Cast 69431. It was extracted after service in the Heysham 1 power station (Reactor 2, Quadrant D, Boiler 1) [19]. This material had been subjected to 65,015 hours of reactor operation at 490-530°C, followed by artificial thermal ageing at 550°C for 22,100 hours [20]. The chemical composition is shown in Table 1 and the average grain size was 74±6 μm [21]. All specimens were taken adjacent to one-another and with the cantilever arms oriented parallel to the axis of parent pipe. The specimens were all from parent material remote from any welds. Previous tests on the same material have shown that it is only weakly textured, with none of the major crystallographic axes exceeding 1.4 Multiples of Random Density (MRD) in any direction [22].

Cr	Ni	Mo	Mn	Si	Co	C	P	S	B	Fe
17.17	11.83	2.19	1.98	0.40	0.10	0.06	0.021	0.014	0.005	Bal.

2.3. Specimen preparation

Six purpose-designed Double Cantilever Beam (DCB) specimens of Type 316H with overall dimensions 80 x 32 x 16 mm were prepared by cutting them from an ex-service forging using wire Electrical Discharge Machining (EDM). M8 loading screws of Nimonic 80A at the mouth of the cantilevers were used to pre-stress the specimens at room temperature, as shown in Figure 1. The screws were gradually tightened while measuring the opening displacement of the cantilever mouth using an Instron 2670-132 extensometer (Instron Corp., Norwood, MA., USA). All specimens were loaded to an opening displacement of 1121±2 µm; FEA results indicated that this would produce a maximum von Mises equivalent stress of 380 MPa at the joined end of the cantilevers. To avoid any strain-hardening which might affect the material's creep deformation rate, the specimens were designed so that only a small amount of plastic deformation would occur at room temperature during screw-loading (see Figure 6). Furthermore, the creep deformation rate for this material is relatively insensitive to room-temperature pre-straining at the levels used here (<1%) [23], [24].
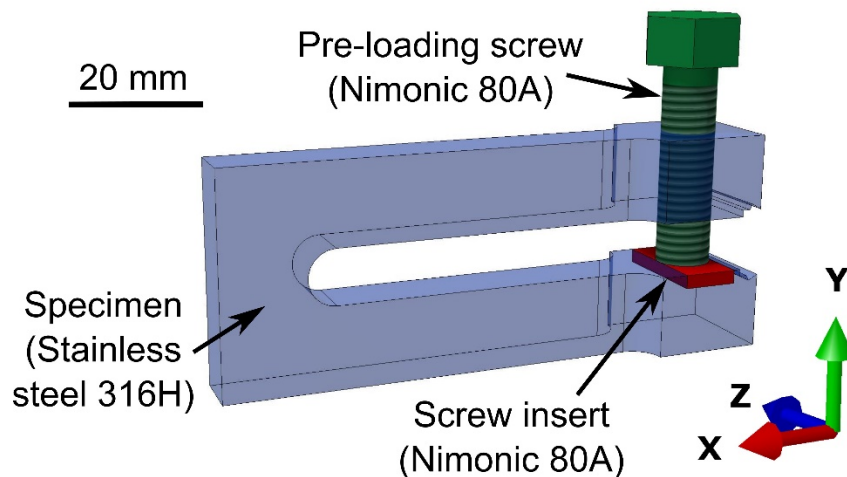

Figure 1: Purpose-designed Double Cantilever Beam (DCB) specimen of Type 316H austenitic stainless steel. This design ensures that the most highly-stressed region is the connection between the beams, and that no localised deformation occurs close to the pre-loading screw.

The specimens were each subjected to high-temperature soaks at 550±3°C in air for different durations: 1, 10, 50, 200 and 800 hours. One control specimen was not heated but instead left in the as-loaded condition. The temperature was monitored using three specimen-contacting K-type thermocouples. The heating of the specimens was performed in a manner which minimised time spent at intermediate temperatures while avoiding a temperature gradient within the specimen. An initial heating rate of 20.5 °C/min was used, and each specimen was left to furnace-cool after the soak resulting in a maximum cooling rate of 1.7 °C/min. The temperature regimes are shown in Figure 2. No external loading was applied to the specimens.

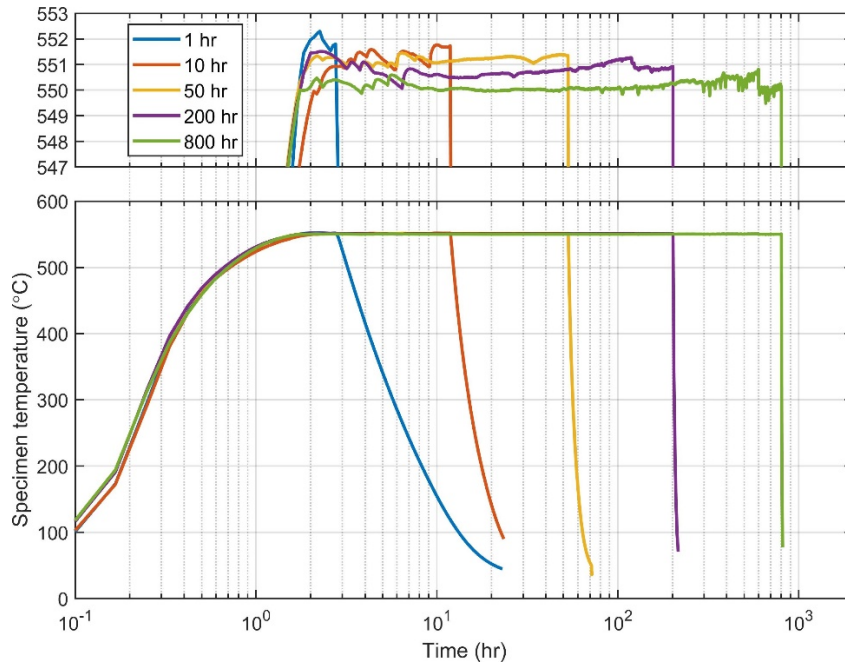*Figure 2: Temperature regimes experienced by the five heated specimens. The specimen temperature was maintained at 550±3°C throughout the soaking period.*

2.4. Finite element modelling

Finite element models of the pre-stressed Double-Cantilever Beam specimens were used to predict the stress relaxation inside them at high temperature. The Abaqus/CAE v6.12 pre-processor and Abaqus/Standard v6.12 FEA solver were used for all models. A domain representing one-quarter of the DCB specimen was created (see Figure 3), with appropriate boundary conditions applied at the symmetry planes. The domain was meshed using 36,345 10-noded quadratic tetrahedron elements (Abaqus type C3D10) resulting in a model with 109,035 degrees-of-freedom. The loading screw was not modelled; instead an imposed displacement was applied to the interior of the screw hole to simulate screw-loading. During heating, a very small additional displacement (roughly 8 μm) was applied to account for the effect of the small difference in the thermal expansion coefficients of Type 316H and the Nimonic 80A loading screw.
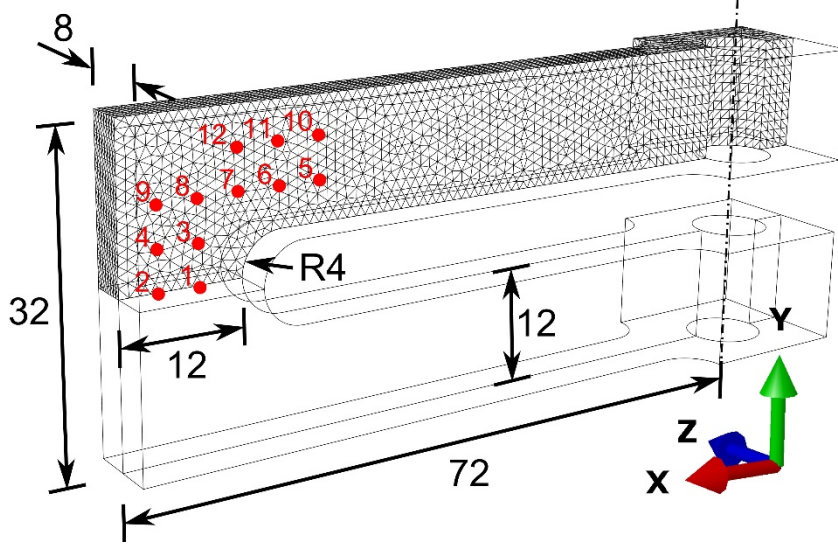
Figure 3: Finite element domain and mesh representing one-quarter of a Double Cantilever beam specimen. Dimensions in mm. The numbered red dots indicate locations where neutron diffraction measurements were performed in the real specimens. The loading screw is not shown.

The material constitutive model used to represent Type 316H included temperature-dependent elastic, plastic and creep behaviour. The elastic behaviour of Type 316H was assumed to be isotropic, with the Poisson's ratio ν taken to be a constant 0.28 and a Young's modulus of E = 205 GPa at 20°C [25]. The rate-independent component of inelastic deformation was modelled using a Chaboche nonlinear isotropic/kinematic hardening law with a single back-stress [26], [27], giving the material's yield surface as:

Equation 1

$$\sqrt{\frac{3}{2}\left(s_{ij} - a_{ij}\right)\left(s_{ij} - a_{ij}\right)} - \sigma^0 = 0$$

where σ^0 is the material's initial yield stress, s_{ij} is the stress deviator tensor and a_{ij} is the backstress deviator tensor:

Equation 2

$$s_{ij} = \sigma_{ij} - \frac{1}{3}\sigma_{kk}\delta_{ij}$$

$$a_{ij} = \alpha_{ij} - \frac{1}{3}\alpha_{kk}\delta_{ij}$$

σ_{ij} and a_{ij} are the stress and backstress tensors, respectively, and δ_{ij} is the Kronecker delta. The change in backstress is evaluated from the backstress rate ($\dot{\alpha}_{ij}$) given by:

Equation 3

$$\dot{\alpha}_{ij} = C\frac{1}{\sigma^0}\left(\sigma_{ij} - \alpha_{ij}\right)\dot{\bar{\varepsilon}}^{pl} - \gamma\alpha_{ij}\dot{\bar{\varepsilon}}^{pl}$$

where $\dot{\bar{\varepsilon}}^{pl}$ is the equivalent plastic strain rate. C and γ are material-dependent hardening parameters. In this study, the hardening parameters and the yield stress σ^0 were also taken to be temperature-

6

dependent (see Table 2) and were determined from elevated-temperature uniaxial cyclic hardening tests [28].

Table 2: Coefficients for an isotropic/kinematic hardening model of AISI/SAE Type 316H austenitic stainless steel in the temperature range $20 - 600°C$ [28].

Temperature T (°C)	Yield stress σ^0 (MPa)	Hardening parameter C (MPa)	Hardening parameter γ
20	351.8	4997.0	34.0
100	289.3	5268.2	34.0
200	242.8	5576.2	34.0
300	220.9	5753.2	34.0
400	213.5	5695.7	34.0
500	211.8	5300.2	34.0
600	205.5	4463.1	34.0

A creep deformation law was included for temperatures above 425°C. Creep deformation in the primary and secondary regimes was assumed to follow the RCC-MR deformation law in a strain-hardening formulation [29–31]. Wang et al. have shown this model performs reasonably well for uniaxial creep stress relaxation of Type 316H [32]:

Equation 4

$$\bar{\varepsilon}_c = C_1 t^{C_2} \bar{\sigma}^{n_1} \qquad \text{for} \qquad 425°C \leq T \leq 700°C \quad \text{and} \quad t \leq t_{fp}$$

$$\bar{\varepsilon}_c = C_1 t_{fp}^{C_2} \bar{\sigma}^{n_1} + 100 C \bar{\sigma}^n (t - t_{fp}) \qquad \text{for} \qquad 480°C < T \leq 700°C \quad \text{and} \quad t > t_{fp}$$

Where $\bar{\varepsilon}_c$ is the equivalent creep strain (in %) and $\bar{\sigma}$ is the equivalent stress. t is the current time and t_{fp} is the time at the transition between primary and secondary creep. The material constants n, n_1, C, C_1 and C_2 are dependent on temperature T. The primary-secondary transition time t_{fp} is given by:

Equation 5

$$t_{fp} = \infty \qquad \text{for} \qquad 425°C \leq T \leq 480°C$$

$$t_{fp} = C_3 \bar{\sigma}^{n_3} \qquad \text{for} \qquad 480°C < T \leq 700°C$$

where:

Equation 6

$$n_3 = \frac{n - n_1}{C_2 - 1}$$

and:

Equation 7

$$C_3 = \left(\frac{100 C}{C_1 C_2} \right)^{\frac{1}{C_2 - 1}}$$

Empirically-derived creep deformation law coefficients for Type 316H (from R66 [29]) are given in Table 3. Although creep coefficients specific to aged ex-service Type 316H have been derived by Wang et al. [19], we used the Table 3 values so that our model would most closely represent what might be used in a real structural integrity assessment. The expressions for equivalent creep strain in Equation

4 were differentiated with respect to time to produce a strain-hardening formulation which was implemented in an Abaqus user subroutine. No creep damage model was used: in the stress relaxation tests, the specimens were expected to experience much smaller creep strains than would be required to initiate damage and tertiary creep.

Table 3: RCC-MR creep deformation model coefficients for 316, 316H and 316LN austenitic stainless steels [29].

Temperature T (°C)	C	C_1	C_2	n	n_1
425	0	0	0.34043	1	3.9073
450	0	7.89E-13	0.34043	1	3.9073
475	5.83E-33	8.73E-13	0.36121	9.78	4.0057
500	2.05E-32	1.21E-12	0.38054	9.97	4.0722
525	4.15E-29	1.88E-12	0.40053	9.06	4.125
550	5.28E-26	2.96E-12	0.42131	8.2	4.18
575	3.66E-25	1.81E-12	0.46417	8.2	4.3952

2.5. Neutron diffraction

To determine the residual stresses remaining in the DCB specimens after high-temperature exposure, time-of-flight neutron diffraction measurements were performed using the ENGIN-X diffractometer at the ISIS Pulsed Neutron Source [33], [34]. The measurement setup is shown in Figure 4. Diffraction measurements were taken at 12 locations in each specimen, as shown in Figure 3. These locations were chosen to cover highly-stressed regions of the specimen while ensuring that the gauge volume would always be located completely inside the material. A gauge volume of 3x3x3 mm^3 was used for all measurements, defined by a pair of slits on the primary beam and by radial secondary collimators. At each location, diffraction measurements were taken with the specimen in 6 different orientations using a goniometer. Since ENGIN-X has two opposing detector banks, this gave access to 11 unique scattering vectors $[l \quad m \quad n]^T$, allowing determination of the lattice parameter for 11 directions at each location - one scattering direction was repeated. The specimens were located on the beamline using a FARO Vantage laser tracker (FARO Technologies, FL., USA) which could locate spherically-mounted retroreflectors attached to the rack holding the specimens. Kinematic calculations required to position the samples were performed using the SScanSS virtual laboratory software [35–37].
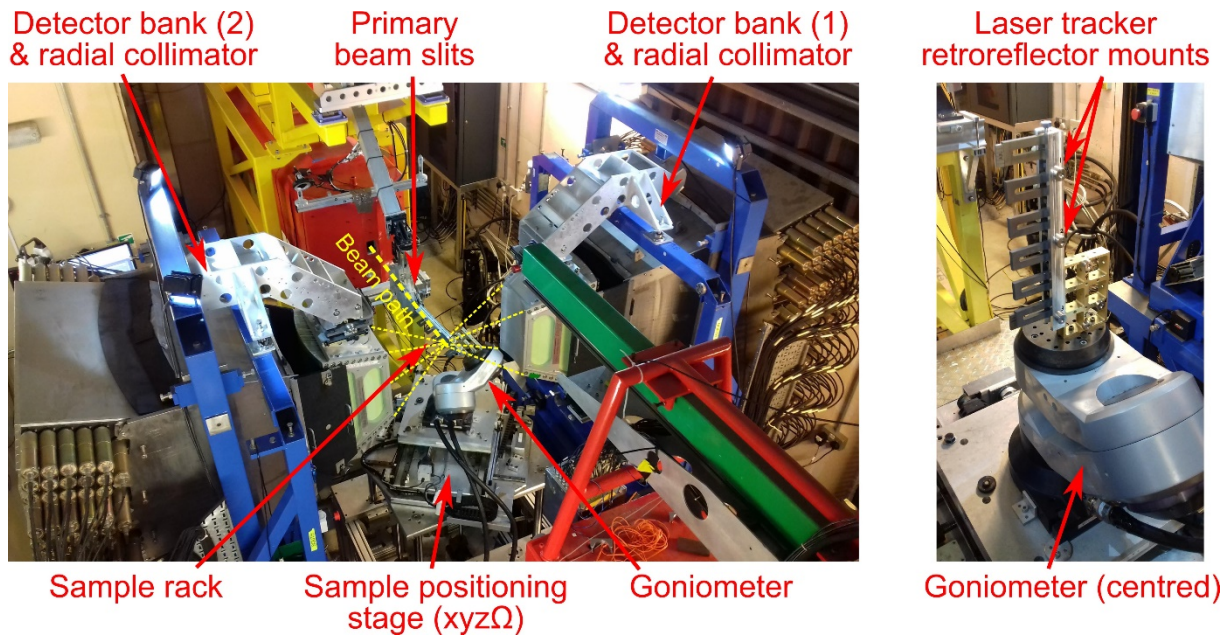
Figure 4: Experimental setup for neutron diffraction measurements on the ENGIN-X diffractometer. The specimens were mounted together in a rack and oriented relative to the neutron optics using a large goniometer and a laser tracker.

Table 4: Scattering angles and direction cosines used to define the measurement directions during the neutron diffraction measurements. The measurement at $\phi = 45°$, $\psi = 0°$ is repeated, so 11 unique strain directions are measured. The measurement directions are shown graphically in Figure 5.

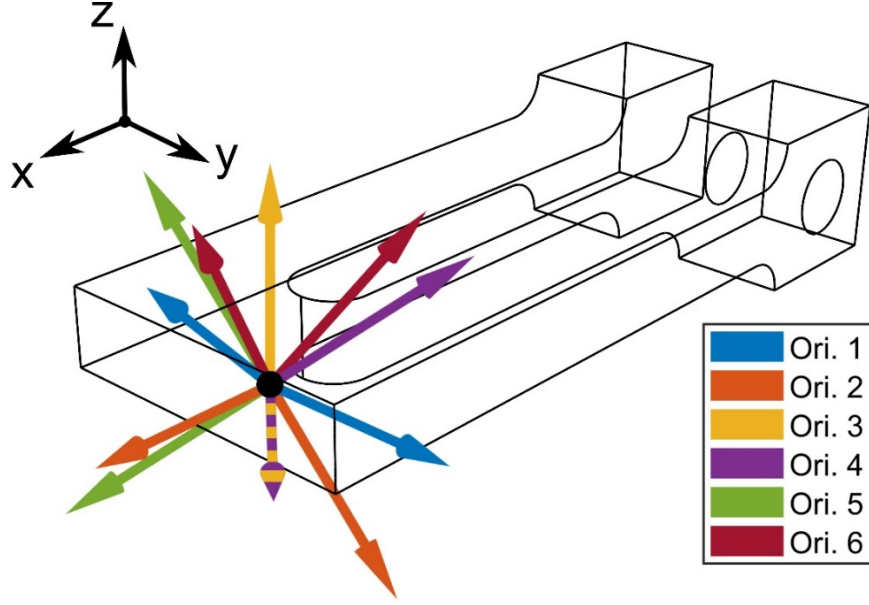| Measurement		Scattering angles		Direction cosines		
Specimen orientation #	Detector bank #	Azimuth ϕ (°)	Elevation ψ (°)	l	m	n
1	1	90	0	0	1	0
1	2	0	45	√2/2	0	√2/2
2	1	0	0	1	0	0
2	2	90	-45	0	-√2/2	-√2/2
3	1	0	90	0	0	1
3	2	45	0	1	0	0
4	1	135	35.26	-√2/2	1/2	1/2
4	2	45	0	1	0	0
5	1	-90	45	0	-√2/2	√2/2
5	2	-45	-35.26	√2/2	1/2	-1/2
6	1	180	26.57	-0.8944	0	0.4473
6	2	0	63.43	0.4473	0	0.8944

Figure 5: Scattering vectors used for neutron diffraction strain measurement. This set of vectors, listed in Table 4, is the set of directions in which strain was measured at each location in each DCB specimen. One strain direction is measured twice (see Orientations 3 and 4).

The GSAS structure refinement package was used to fit the diffraction data using a Pawley-type refinement and hence determine the lattice parameter (a^{lmn}) from each measurement in a direction $[l \quad m \quad n]^T$ [38]. Comb specimens cut using EDM from the same Type 316H material were used to determine the material's unstrained lattice parameter (a_0^{lmn}) in the same manner [39]. Separate unstrained lattice parameter measurements were used for each direction. Elastic strains were calculated from the lattice parameters using:

Equation 8

$$\varepsilon^{lmn} = \frac{a^{lmn} - a_0^{lmn}}{a_0^{lmn}}$$

where ε^{lmn} is the elastic strain for the measured direction. Using these strain results, we determined the complete elastic strain tensor at each measured location. The 6 independent components of the strain tensor can be related to each strain measurement using the strain transformation equation [40–42]:

Equation 9

$$\varepsilon^{lmn} = \varepsilon_{11} \sin^2 \psi \cos^2 \phi + \varepsilon_{22} \sin^2 \psi \sin^2 \phi + \varepsilon_{33} \cos^2 \phi + 2\varepsilon_{12} \sin^2 \psi \sin \phi \cos \phi + 2\varepsilon_{23} \sin \psi \cos \psi \sin \phi + 2\varepsilon_{13} \sin \psi \cos \psi \cos \phi$$

where ε_{11}, ε_{12} etc. are components of the strain tensor, ϕ is the azimuth (measured anticlockwise about the sample z-axis from the x-axis), and ψ is the elevation (measured clockwise about the sample y′-axis). Therefore, with 11 measurements it was possible to construct and solve an over-determined system of simultaneous linear equations to find the elastic strain tensor [43–45]:

Equation 10

$$\varepsilon_i = A_{ij}^+ \varepsilon_j^{lmn}$$

where ε_i are the independent components of the elastic strain tensor expressed as a 6-element vector, ε_j^{lmn} is a set of directional strain measurements ($i = 1:11$ here), A_{ji} is the corresponding matrix of direction cosines (from Equation 9) and A_{ij}^+ is its pseudo-inverse. After determining the elastic strain tensor at each location, the stress tensors were determined using Hooke's law for an isotropic material:

Equation 11

$$\sigma_{ij} = 3K\left(\frac{1}{3}\varepsilon_{kk}\delta_{ij}\right) + 2G\left(\varepsilon_{ij} - \frac{1}{3}\varepsilon_{kk}\delta_{ij}\right)$$

where σ_{ij} is the (Cauchy) stress tensor, ε_{ij} is the elastic strain tensor, K is the material's bulk modulus:

Equation 12

$$K = \frac{E}{3(1 - 2\nu)}$$

and G is the shear modulus:

Equation 13

$$G = \frac{E}{2(1 + \nu)}$$

The material's continuum-scale Young's modulus and Poisson's ratio were used (E = 205 GPa and ν = 0.28, respectively) as these are appropriate for relating macrostrains from full-pattern refinement of neutron diffraction data with the corresponding macroscopic stresses [46].

2.6. Measurement uncertainty

The uncertainty in the determination of lattice parameter by neutron diffraction was estimated from the goodness-of-fit of the Pawley refinement. For each measurement, the estimated standard deviations of the lattice parameter (Δa^{lmn}) and unstrained lattice parameter (Δa_0^{lmn}) were used to estimate the uncertainty in the measured strains [47]:

Equation 14

$$\Delta\varepsilon^{lmn} \cong \frac{1}{a_0^{lmn}}\sqrt{(\Delta a^{lmn})^2 + \left(\Delta a_0^{lmn}\right)^2}$$

To determine the uncertainties of the strain tensor components, the uncertainties in measured strains were propagated through the system of simultaneous linear equations used to find the elastic strain tensor (Equation 10). The variance-covariance matrix of the tensor components ($\Sigma_{ij}^{\varepsilon}$) is:

Equation 15

$$\text{var}(\varepsilon_i) = \Sigma_{ij}^{\varepsilon} = A_{ik}^+ \Sigma_{kl}^{\varepsilon lmn} A_{jl}^+$$

where $\Sigma_{kl}^{\varepsilon lmn}$ is the variance-covariance matrix of the measured strains. If the measurement uncertainties are uncorrelated then this reduces to:

Equation 16

$$\text{var}(\varepsilon_i) = \Sigma_{ij}^{\varepsilon} = A_{ik}^+ \Sigma_{k}^{\varepsilon lmn} A_{jk}^+$$

where $\Sigma_{k}^{\varepsilon lmn}$ is the variance of the kth measured strain:

Equation 17

$$\Sigma_k^{\varepsilon^{lmn}} = \left(\Delta\varepsilon_k^{lmn}\right)^2$$

Further assuming that the calculated strain tensor components are uncorrelated, i.e. that $\Sigma_{ij}^{\varepsilon}$ is diagonal, the uncertainties in the strain tensor were propagated through Hooke's law to give an estimate of the uncertainty in the resulting stress tensor, as described by Wimpory et al. [47], [48].

This method of uncertainty estimation only considers uncorrelated random errors resulting from structure refinement of the diffraction data. It ignores any uncertainty in strain resulting from systematic errors, including sample positioning errors, inappropriate unstrained lattice parameter specimens, or material anisotropy. It also assumes that the material can be considered elastically isotropic. In general, however, there may be a more complex relationship between the macroscopic stress tensor and the strain measurements [49].

3. Results

3.1. Finite Element Analysis

The results of FEA (see Figure 6) indicated that after loading-up of the specimens, the maximum equivalent stress in each specimen would reach 382 MPa at the interior radius of region ②. They also showed that a small amount of plastic deformation would occur at this inner radius during loading: 1.39×10^{-3} equivalent strain. Some plasticity in regions ② and ③ occurred during the initial heating-up of the specimens: e.g. in region ② a further 2.23×10^{-3} equivalent plastic strain occurs, accompanied by a reduction in the maximum equivalent stress of -154 MPa.

The model also predicted that significant relaxation of residual stress will occur due to creep during the high-temperature soak. The distribution of accumulated equivalent creep strain is shown in Figure 6i-l: as expected, the creep strain is localised to areas of initially-high equivalent stress (①, ② and ③). In these stress-relaxation tests, the stress reduces as creep strain accumulates. Only a small amount of creep strain, comparable to the initial elastic strain, is required to cause significant stress relaxation. Therefore, the equivalent creep strain predicted by FEA is relatively low even after 800 hr of exposure, with a maximum equivalent strain of 3.6×10^{-3} occurring in region ②. The stress field in the sample redistributes significantly as plasticity and creep occur. For example, the stress in region ④ reduces during the high-temperature soak even though no creep strain occurs there.
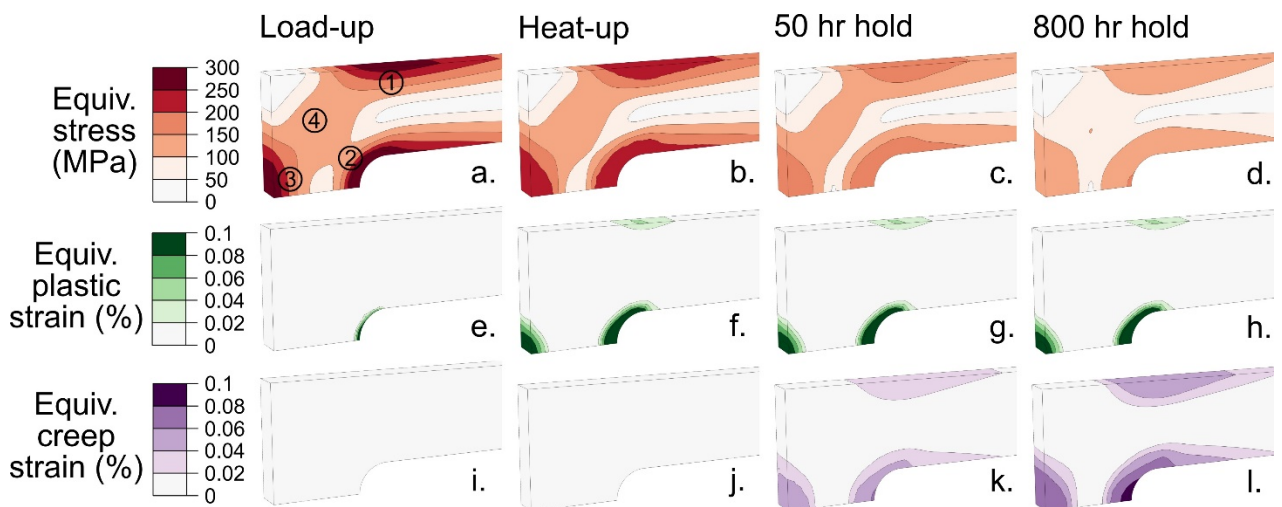

Figure 6: Predicted evolution of stress (a-d), plastic strain (e-h) and creep strain (i-l) in the 800 hr hold specimen, from FEA. von Mises equivalent values of stress and strain are shown. Initial stress relaxation due to reduction in the short-term elastic limit occurs during the heat-up, and further relaxation due to creep occurs during the hold.

Figure 7 shows how the σ_{11} (x-direction) and σ_{22} (y-direction) components of the stress tensor at the 12 labelled points in Figure 3 change over time. At all locations where a large change in stress occurs, the different components of the stress tensor do not change in proportion to one another: the unloading path during stress relaxation is strongly non-radial. This occurs because the stress is not initially uniform throughout the structure and it redistributes in response to localised creep (as shown in Figure 6). Areas with an initially high effective stress deform faster, shedding load to areas of initially lower effective stress.
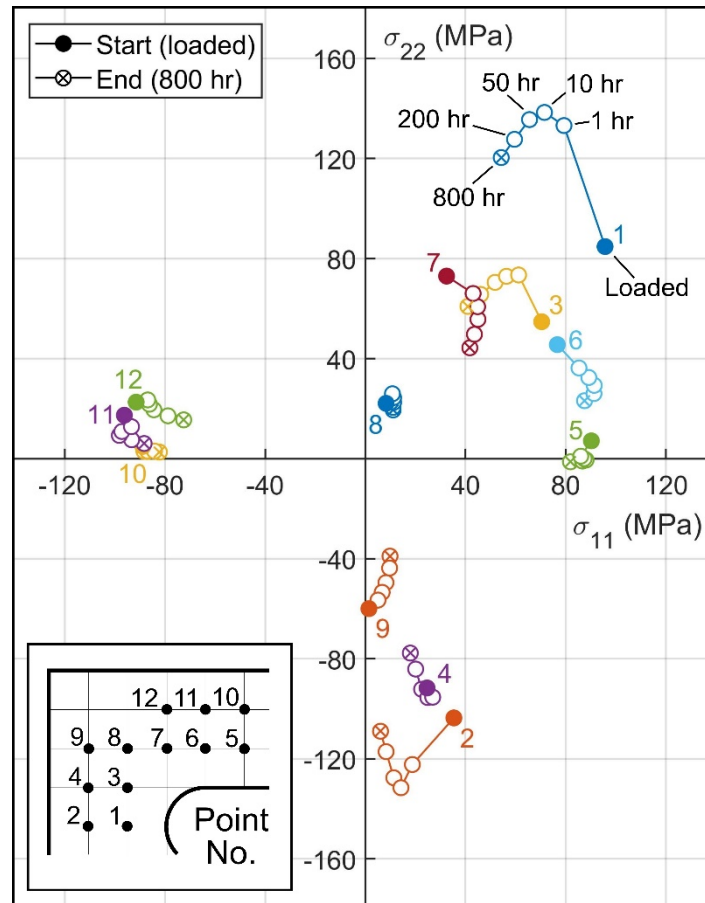
Figure 7: Predicted stress trajectories at 12 locations in a Type 316H DCB specimen undergoing creep stress relaxation. The σ_{11} (sample x-direction) and σ_{yy} (sample y-direction) stresses are shown, although other stress tensor components may also be significant. None of the stress trajectories are radial to the origin: strongly non-proportional changes in the stress tensor occur at most locations.

3.2. Neutron diffraction

Figure 8 shows the principal stresses and directions measured at 12 locations in a specimen of Type 316H, and the corresponding quantities predicted by FEA. The specimen is clearly in a state of bending: the principal stress components on either side of the specimens' neutral axis have opposite signs. The rotation of the stress tensor in the transition between the arm and the end of the specimen is clearly visible, and some locations are in a state of almost pure shear with respect to the specimen coordinate system. For example, the point circled in magenta in Figure 8a (Point #8) initially experiences the following stress state:

Equation 18

$$\sigma_{ij}^{8,init.} = \begin{bmatrix} 9.6 \pm 5.3 & 68.8 \pm 3.0 & -3.6 \pm 2.6 \\ & 10.3 \pm 5.8 & -8.7 \pm 2.9 \\ symm. & & 11.5 \pm 5.0 \end{bmatrix} \text{ MPa}$$

i.e. approximately pure shear in the x-y plane. Whereas the point on the bending arm circled in cyan (Point #5) experiences almost pure uniaxial tension:

Equation 19

$$\sigma_{ij}^{5,init.} = \begin{bmatrix} 93.2 \pm 5.0 & 1.9 \pm 2.9 & -5.5 \pm 2.4 \\ & -12.4 \pm 5.2 & 4.3 \pm 2.6 \\ symm. & & 3.5 \pm 4.7 \end{bmatrix} \text{MPa}$$

The out-of-plane components of stress ($\sigma_{33}, \sigma_{23}, \sigma_{13}$) were found to be small for all specimen conditions and measurement locations. This is expected, as all the measurement points lie on the specimens' x-y symmetry plane. Figure 8 also shows very good agreement between the experiment and the model, although in some locations the measured principal stress directions are slightly rotated with respect to the FEA result. Both the experimental and FEA results show some stress redistribution during the initial high-temperature exposure (up to 1 hr) resulting from the reduction in short-term elastic limit, and then gradual relaxation over the hold period (1 hr → 800 hr).
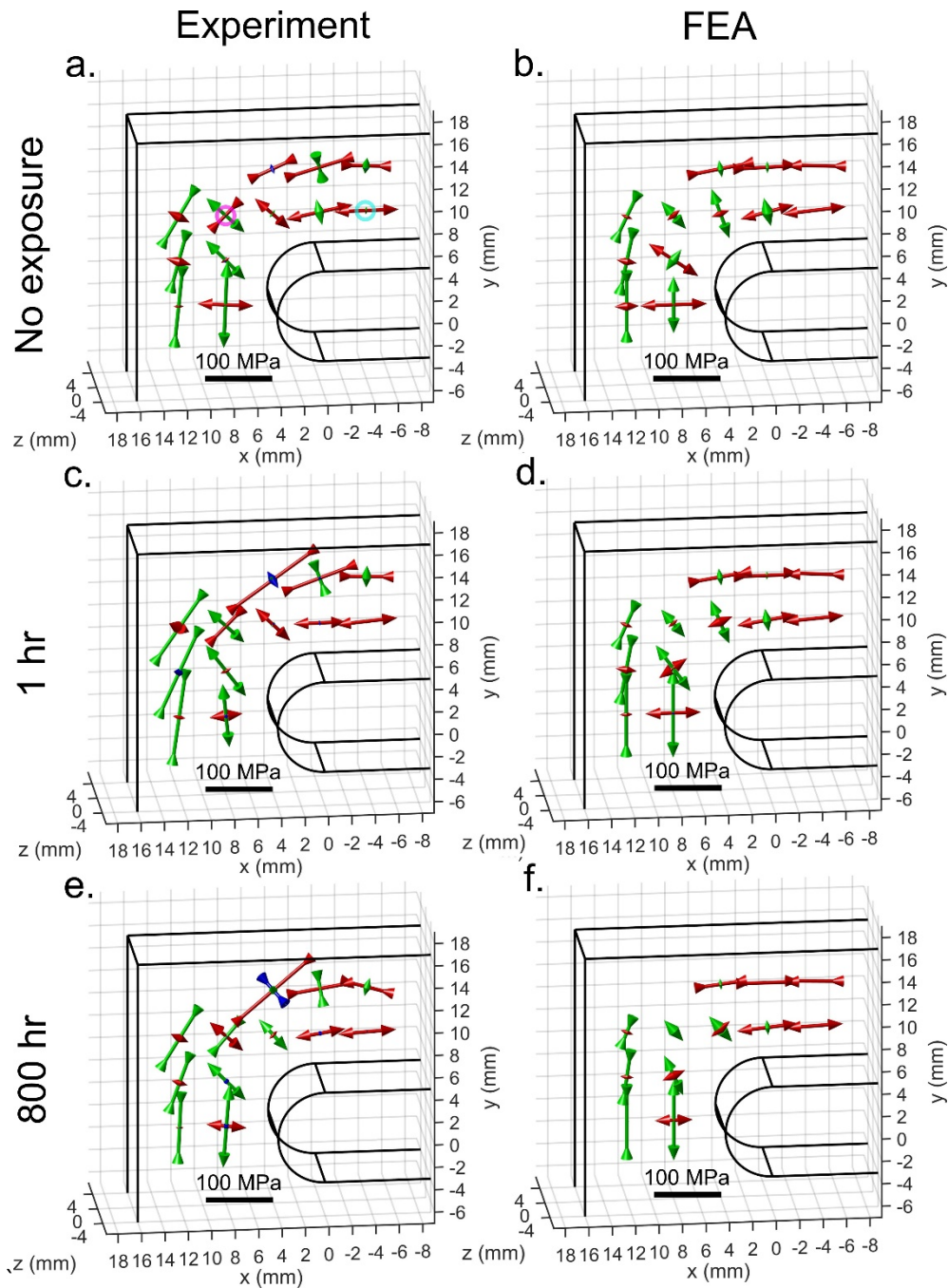
Figure 8: Principal stresses in pre-stressed Double-Cantilever Beam specimens of Type 316H stainless steel measured using neutron diffraction (a,c,e), with corresponding FEA results (b,d,f). Outwards-tipped arrows indicate tension, inwards-tipped arrows indicate compression. Red arrows indicate the principal stress closest to the sample x direction, green is closest to y and blue is closest to z. The principal stress closest to the out-of-plane (z) direction is very small in most cases.

The equivalent stress at each of the 12 measurement locations was also calculated from the experimental and FEA results, and the mean equivalent stress for each specimen was found. This was used to produce the time series shown in Figure 9. This shows that gradual relaxation of the residual stress field occurs over time. Although the measured stress field has a slightly greater magnitude of equivalent stress than that predicted by FEA on average, the rate of stress field relaxation is very similar: both showing ~15 MPa relaxation over the entire period.

15
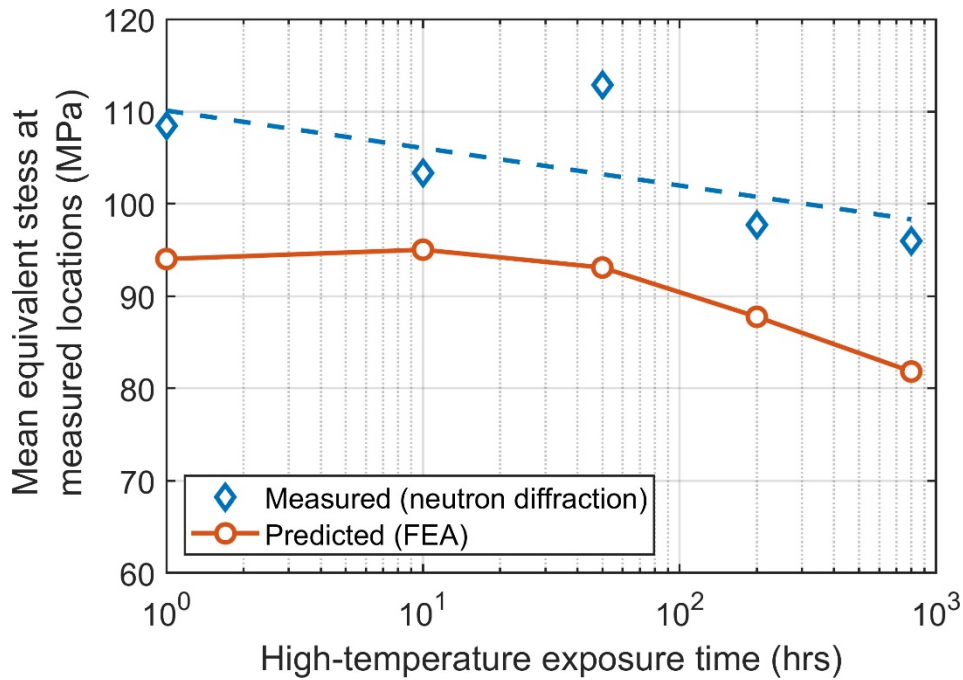
Figure 9: Equivalent stress (mean for all 12 measured locations in a specimen) after cooling as a function of high-temperature exposure. The FE model slightly under-predicts the final stresses, although the rate of stress reduction over time is similar to that indicated by the ND results.

4. Discussion

4.1. Validation of multiaxial creep deformation laws

The specimens in this study were relatively lightly-stressed: the neutron diffraction results from the samples subjected to a 1 hr hold (Figure 8) indicate that after heating-up, equivalent stresses in the range 74 MPa to 155 MPa occur at the measurement locations. The magnitude of creep stress relaxation observed in the experiments was quite small, and slightly less than predicted by the FE models. This suggests that either the primary and secondary creep deformation law used for modelling (i.e. the RCC-MR law with R66 material coefficients) is generally conservative, or that the ex-service Type 316H material used here, and which has undergone prior ageing, has been significantly hardened prior to the experiment. This is in agreement with previous work by Wang et al. [32], which also showed that in this lightly-stressed regime at 550°C, the conventional RCC-MR creep coefficients predict higher strain rates than actually occur for ex-service Type 316H.

The magnitude of creep stress relaxation experienced by the specimens here was too small to draw strong conclusions about the role of the equivalent stress in primary/secondary creep deformation laws, but was in line with Type 316H 550°C stress relaxation data presented by Douglas et al. for uniaxial tests [50]. However, the measured stress relaxation was similar to that predicted by FE; this is shown in terms of the point-wise equivalent stress in Figure 10. Also, the experimental results clearly demonstrate that measuring multiaxial creep stress relaxation using ex-situ specimens is feasible. Figure 8 illustrates that the principal stress directions and magnitudes can be established experimentally, as can the equivalent stress at each measurement location; so the creep relaxation of an arbitrarily-complex stress field can be observed directly. This is particularly valuable for studying multiaxial stress relaxation because this process involves stresses which can change over time in a non-proportional way (see Figure 7); diffraction provides a means to measure this non-proportional change. Likewise, general experiments of this type, where arbitrary stress states can be observed, may be used to study the effects of stress mode and material anisotropy on creep deformation [8].
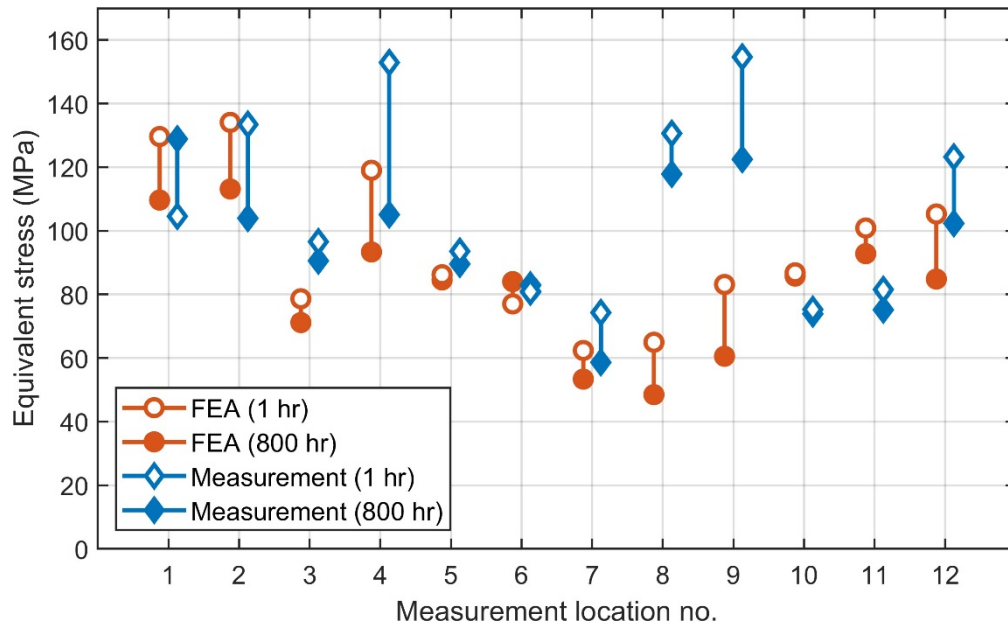
16

Figure 10: Equivalent stress at the 12 measurement locations in DCB specimens of Type 316H austenitic stainless steel after 1 hr and 800 hr soaks at 550°C. Results from Finite Element Analysis and neutron diffraction measurements are compared. The locations of each measurement are indicated in Figure 3.

4.2. Complete stress tensors from neutron diffraction

At each measurement location within each sample, the elastic strain in 11 directions was determined using neutron diffraction. The six independent components of the elastic strain tensor were calculated from these measurements. With 11 measurements at each location, the system of strain rotation equations which relates the strain measurements to the tensor components (Equation 10) is over-determined. Consequently, the strain tensor can be found with a greater degree of certainty than is present for any of the individual measurements. This is illustrated in Figure 11, which shows normalised histograms of the standard uncertainties in the 846 strain measurements and the resulting 432 strain tensor components. The mean uncertainty in strain tensor components (17.6 με) is less than the mean uncertainty in the measurements (24.6 με), so the histogram for tensor components is shifted to the left.
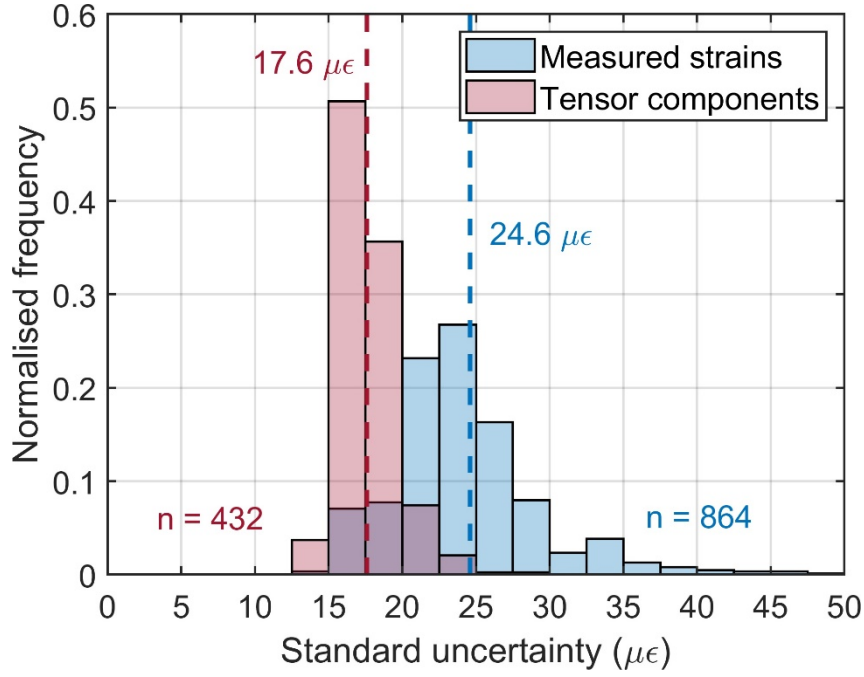
17

Figure 11: Uncertainty in individual elastic strain values measured from the specimens using neutron diffraction (12 per location) and the components of the strain tensor inferred from these measurements (6 per location). Dashed lines show the locations of the means. Over-determination of the strain tensor at each location produces reduced uncertainty.

This uncertainty analysis assumes that any errors in the strain measurements are normally distributed and that there is no co-variance between measurements. In fact, the measurements may be affected by common sources of error. The analysis also assumes that the continuum-scale strain rotation relationship (Equation 9) accurately describes the relationship between the measured strains. Nevertheless, this technique of taking redundant measurements to over-determine the strain tensor is useful in situations where high strain precision is needed, either in one strain tensor component or all of them. For example, it could be used for investigating stresses in specimens made from very stiff materials such as ceramics carbon-based nanocomposites where the range of elastic strains is small, or (as in this study) in metals operating in low stress regimes e.g. creep and superplastic forming. Sampling the lattice spacing in different directions, as done here, is beneficial from a continuum mechanics point-of-view because it ensures that the macro-scale stress tensor is determined from measurements from a larger fraction of the crystallites present within the neutron diffraction gauge volume.

Multiple neutron diffraction measurements can also be used to determine the principal stress directions at a measurement location within a polycrystalline specimen (see Figure 8). This is useful in situations where the principal stress directions are not known and cannot be guessed, e.g. from specimen symmetry. It is particularly significant because many models of plasticity and viscoplasticity depend on the von Mises equivalent stress ($\sigma_{vm} = \sqrt{3J_2}$) and determining the invariants of the stress deviator tensor (J_2 and J_3) requires either the complete stress tensor or the three principal stresses:

Equation 20

$$J_2 = \frac{1}{2} s_{ij} s_{ji}$$

and:

18

$$J_3 = \frac{1}{3} s_{ij} s_{jk} s_{ki}$$

where s_{ij} is the stress deviator tensor. Therefore, full-tensor measurement of stress (residual or applied) could be used to provide validation for models of a wide range of 3D inelastic deformation phenomena - not only models of primary and secondary creep. Currently, neutron diffraction and synchrotron x-ray diffraction are the only methods by which it would be feasible to measure the complete macro-scale stress tensor inside a metal undergoing an unknown inelastic deformation.

5. Conclusions

- Spatially-resolved measurements of the macroscopic stress and strain tensors in complex-shaped samples are possible using neutron diffraction. However, accurate sample positioning is necessary: in this study, a laser tracker and virtual lab environment software (SScanSS) were used successfully to position specimens.

- Measurements of this type can be used to study deformation phenomena in materials in 3D, i.e. with no *a priori* assumptions about the stress state occurring in the material (multiaxiality) or how it changes during the process being investigated (non-proportionality).

- By using multiple neutron diffraction measurements in different directions at the same location to provide over-determination the strain tensor, it is possible to achieve a reduced uncertainty in the stress tensor. However, this technique can only reduce the effects of the non-covariant component of measurement uncertainty.

- The strain-hardening formulation of the RCC-MR/R66 multiaxial creep deformation law for Type 316H stainless steel is conservative for the ex-service material tested here. Relatively little stress relaxation was observed experimentally, and this was slightly less than was predicted by inelastic FEA using the RCC-MR deformation law.

6. Acknowledgements

7. Data availability statement

Raw and analysed neutron diffraction data and finite element modelling results supporting the findings of this article can be accessed at: INSERT DOI LINK AFTER ACCEPTANCE

8. References

[1]   E. Nonbøl, "Description of the Advanced Gas Cooled type of ractor (AGR)," Nordisk Kernesikkerhedsforskning (NKS), N, 1996.

[2]   M. P. Petkov, J. Hu, and A. C. F. Cocks, "Self-consistent modelling of cyclic loading and relaxation in austenitic 316H stainless steel," *Philosophical Magazine*, vol. 99, no. 7, pp. 789–834, 2019.

[3]   S. Hossain, C. E. Truman, D. J. Smith, R. L. Peng, and U. Stuhr, "A study of the generation and creep relaxation of triaxial residual stresses in stainless steel," *International Journal of Solids and Structures*, vol. 44, no. 9, pp. 3004–3020, 2007.

[4] G. A. Webster, S. R. Holdsworth, M. S. Loveday, K. Nikbin, I. J. Perrin, H. Purper, R. P. Skelton, and M. W. Spindler, "A Code of Practice for conducting notched bar creep tests and for interpreting the data," *Fatigue and Fracture of Engineering Materials and Structures*, vol. 27, no. 4, pp. 319–342, 2004.

[5] S. Hossain, C. E. Truman, and D. J. Smith, "Generation of residual stress and plastic strain in a fracture mechanics specimen to study the formation of creep damage in type 316 stainless steel," *Fatigue and Fracture of Engineering Materials and Structures*, vol. 34, pp. 654–666, 2011.

[6] "R5: Assessment Procedure for the High Temperature Response of Structures, Issue 3," EDF Energy Nuclear Generation Ltd., 2012.

[7] M. W. Spindler, "The Multiaxial Creep of Austenitic Stainless Steels," Nuclear Electric, 1994.

[8] H. Altenbach, "Topical problems and applications of creep theory," *International Applied Mechanics*, vol. 39, no. 6, pp. 631–655, 2003.

[9] N. S. Ottosen and M. Ristinmaa, "Creep and Viscoplasticity," in *The Mechanics of Constitutive Modeling*, Elsevier, 2005, pp. 387–421.

[10] J. T. Boyle and J. Spence, "Creep under multiaxial states of stress," in *Stress Analysis for Creep*, Butterworths, 1983, pp. 39–62.

[11] J. A. Francis, W. Mazur, and H. K. D. H. Bhadeshia, "Type IV cracking in ferritic power plant steels," *Materials Science and Technology*, vol. 22, no. 12, pp. 1387–1395, 2006.

[12] I. J. Perrin and D. R. Hayhurst, "Continuum damage mechanics analyses of type IV creep failure in ferritic steel crossweld specimens," *International Journal of Pressure Vessels and Piping*, vol. 76, no. 9, pp. 599–617, 1999.

[13] A. Zolochevsky and G. Z. Voyiadjis, "Theory of creep deformation with kinematic hardening for materials with different properties in tension and compression," *International Journal of Plasticity*, vol. 21, no. 3, pp. 435–462, 2005.

[14] A. C. F. Cocks and M. F. Ashby, "Intergranular fracture during power-law creep under multiaxial stresses," *Metal Science*, vol. 14, pp. 395–402, 1980.

[15] M. W. Spindler, "The multiaxial creep ductility of austenitic stainless steels," *Fatigue and Fracture of Engineering Materials and Structures*, vol. 27, no. 4, pp. 273–281, 2004.

[16] J. T. Boyle and K. Nakamura, "The assessment of elastic follow-up in high temperature piping systems - overall survey and theoreticall aspects," *International Journal of Pressure Vessels and Piping*, vol. 29, pp. 167–194, 1987.

[17] Y. Sakanashi, S. Gungor, A. N. Forsey, and P. J. Bouchard, "Measurement of creep deformation across welds in 316H stainless steel using Digital Image Correlation," *Experimental Mechanics*, vol. 5, pp. 231–244, 2017.

[18] M. van Rooyen and T. H. Becker, "High-temperature tensile property measurements using digital image correlation over a non-uniform temperature field," *Journal of Strain Analysis for Engineering Design*, vol. 53, no. 3, pp. 117–129, 2018.

[19] Y. Q. Wang, H. E. Coules, C. E. Truman, and D. J. Smith, "Effect of elastic follow-up and ageing on the creep of an austenitic stainless steel," *International Journal of Solids and Structures*, vol. 135, pp. 219–232, 2018.

[20] B. Chen, "Effects of Thermo-Mechanical History on Creep Damage in 316H Austenitic Stainless Steel," University of Bristol, 2011.

[21] B. Chen, D. J. Smith, P. E. Flewitt, and M. W. Spindler, "Constitutive equations that describe creep stress relaxation for 316H stainless steel at 550°C," *Materials at High Temperatures*, vol. 28, no. 3, pp. 155–164, 2011.

[22] B. Chen, J. N. Hu, Y. Q. Wang, S. Kabra, A. C. F. Cocks, D. J. Smith, and P. E. J. Flewitt, "Internal strains between grains during creep deformation of an austenitic stainless steel," *Journal of Materials Science*, vol. 50, no. 17, pp. 5809–5816, 2015.

[23] A. Mehmanparast, C. M. Davies, D. W. Dean, and K. Nikbin, "Effects of plastic pre-straining level on the creep deformation, crack initiation and growth behaviour of 316H stainless steel," *International Journal of Pressure Vessels and Piping*, vol. 141, pp. 1–10, 2016.

[24] D. F. Li, N. P. O'Dowd, C. M. Davies, and K. M. Nikbin, "A review of the effect of prior inelastic deformation on high temperaturemechanical response of engineering alloys," *International Journal of Pressure Vessels and Piping*, vol. 87, pp. 531–542, 2010.

[25] B. Chen, J. N. Hu, P. E. J. Flewitt, D. J. Smith, A. C. F. Cocks, and S. Y. Zhang, "Quantifying internal stress and internal resistance associated with thermal ageing and creep in a polycrystalline material," *Acta Materialia*, vol. 67, pp. 207–219, 2014.

[26] J. L. Chaboche, "Constitutive equations for cyclic plasticity and cyclic viscoplasticity," *International Journal of Plasticity*, vol. 5, no. 3, pp. 247–302, 1989.

[27] J. L. Chaboche, "Time-independent constitutive theories for cyclic plasticity," *International Journal of Plasticity*, vol. 2, no. 2, pp. 149–188, 1986.

[28] H. Keinänen, "Variation of Residual Stresses in Aged Components (VORSAC) Task 2.5.4 report: Isotropic-Kinematic Hardening Models," VTT, VALC663, 1999.

[29] C. D. Hamm, "R66 AGR Materials data handbook," British Energy Generation Ltd, 2011.

[30] "RCC-MR, Design and Construction Rules for Mechanical Components of FBR Nuclear Islands, Section 1, Sub-section Z, Technical Appendix A3.," AFCEN, 1985.

[31] "RCC-MR, Design and Construction Rules for Mechanical Components of FBR Nuclear Islands, Section 1, Sub-section Z, Technical Appendix A3.," AFCEN, 2007.

[32] Y. Q. Wang, M. W. Spindler, C. E. Truman, and D. J. Smith, "Critical analysis of the prediction of stress relaxation from forward creep of Type 316H austenitic stainless steel," *Materials and Design*, vol. 95, pp. 656–668, 2016.

[33] J. R. Santisteban, M. R. Daymond, J. A. James, and L. Edwards, "ENGIN-X: A third-generation neutron strain scanner," *Journal of Applied Crystallography*, vol. 39, no. 6, pp. 812–825, 2006.

[34] S. Y. Zhang, A. Evans, E. Eren, B. Chen, M. Pavier, Y. Wang, S. Pierret, R. Moat, and B. Mori, "ENGIN-X - instrument for materials science and engineering research," *Neutron News*, vol. 24, no. 3, pp. 22–26, 2013.

[35] J. A. James and L. Edwards, "Application of robot kinematics methods to the simulation and control of neutron beam line positioning systems," *Nuclear Instruments and Methods in Physics Research, Section A: Accelerators, Spectrometers, Detectors and Associated Equipment*, vol. 571, no. 3, pp. 709–718, 2007.

[36] S. O. Nneji, S. Y. Zhang, S. Kabra, R. J. Moat, and J. A. James, "Modelling and control of neutron and synchrotron beamline positioning systems," *Nuclear Instruments and Methods in Physics Research A*, vol. 813, pp. 123–131, 2016.

[37] S. O. Nneji, "Development of a Robotic Positioning and Tracking System for a Research Laboratory," The Open University, 2017.

[38] A. C. Larson and R. B. V. Dreele, "General Structure Analysis System (GSAS)," Los Alamos National Laboatory, LAUR 86-748, 2004.

[39] P. J. Withers, M. Preuss, A. Steuwer, and J. W. L. Pang, "Methods for obtaining the strain-free lattice parameter when using diffraction to determine residual stress," *Journal of Applied Crystallography*, vol. 40, no. 5, pp. 891–904, 2007.

[40] T. M. Holden, "Neutron Diffraction," in *Practical Residual Stress Measurement Methods*, 1st ed., G. S. Schajer, Ed. Wiley, 2013.

[41] I. C. Noyan and J. B. Cohen, *Residual stress - measurement by diffraction and interpretation*. Springer, 1987.

[42] R. A. Winholtz, "Characterization of macrostress," in *Analysis of residual stress by diffraction using neutron and synchrotron radiation*, M. E. Fitzpatrick and A. Lodini, Eds. Taylor and Francis, 2003, pp. 60–77.

[43] H. E. Coules, G. C. M. Horne, S. Kabra, P. Colegrove, and D. J. Smith, "Three-dimensional mapping of the residual stress field in a locally rolled aluminium alloy specimen," *Journal of Manufacturing Processes*, vol. 26, pp. 240–251, 2017.

[44] H. G. Priesmeyer and J. Schroder, "Strain tensor determination using neutron diffraction," in *Shot peening - Theory and application*, J. S. Eckersey and J. Champaigne, Eds. IITT-International, 1991, pp. 95–100.

[45] J. S. Robinson, D. J. Hughes, and C. E. Truman, "Confirmation of principal residual stress directions in rectilinear components by neutron diffraction," *Strain*, vol. 47, no. Suppl. 2, pp. 36–42, 2011.

[46] M. R. Daymond, M. A. M. Bourke, R. B. V. Dreele, B. Clausen, and T. Lorentzen, "Use of Rietveld refinement for elastic macrostrain determination and for evaluation of plastic strain history from diffraction spectra," *Journal of Applied Physics*, vol. 82, no. 4, pp. 1554–1562, 1997.

[47] R. C. Wimpory, C. Ohms, M. Hofmann, R. Schneider, and A. G. Youtsos, "Statistical analysis of residual stress determinations using neutron diffraction," *International Journal of Pressure Vessels and Piping*, vol. 86, no. 1, pp. 48–62, 2009.

[48] R. C. Wimpory, C. Ohms, M. Hofmann, R. Schneider, and A. G. Youtsos, "Corrigendum to "Statistical analysis of residual stress determinations using neutron diffraction," *International Journal of Pressure Vessels and Piping*, vol. 86, no. 10, p. 721, 2009.

[49] I. C. Noyan, J. R. Bunn, M. K. Tippett, E. A. Payzant, B. Clausen, and D. W. Brown, "Experimental determination of precision, resolution, accuracy and trueness of time-of-flight neutron diffraction strain measurements," *Journal of Applied Crystallography*, vol. 53, pp. 494–511, 2020.

[50] J. Douglas, M. Spindler, and R. Dennis, "Development of an advanced creep model for Type 316 stainless steel," in *Proceedings of the 8th International Conference on Creep and Fatigue at Elevated Temperatures (CREEP8)*, 2007, p. 26152.
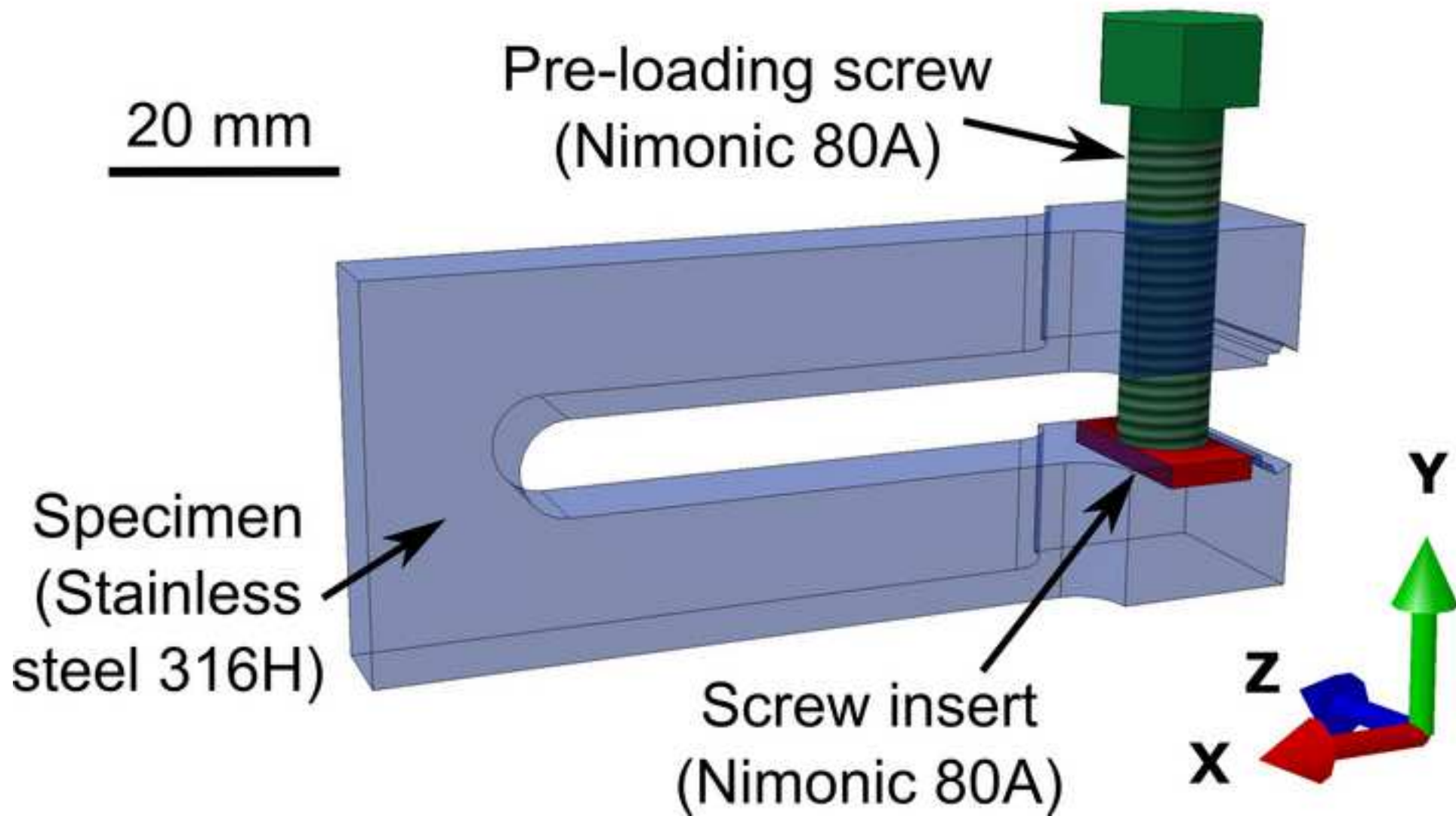
20 mm

Pre-loading screw
(Nimonic 80A)

Specimen
(Stainless
steel 316H)

Screw insert
(Nimonic 80A)

Figure 4

Detector bank (2) & radial collimator

Primary beam slits

Detector bank (1) & radial collimator

Laser tracker retroreflector mounts

Beam path

Sample rack

Sample positioning stage (xyzΩ)

Goniometer

Goniometer (centred)
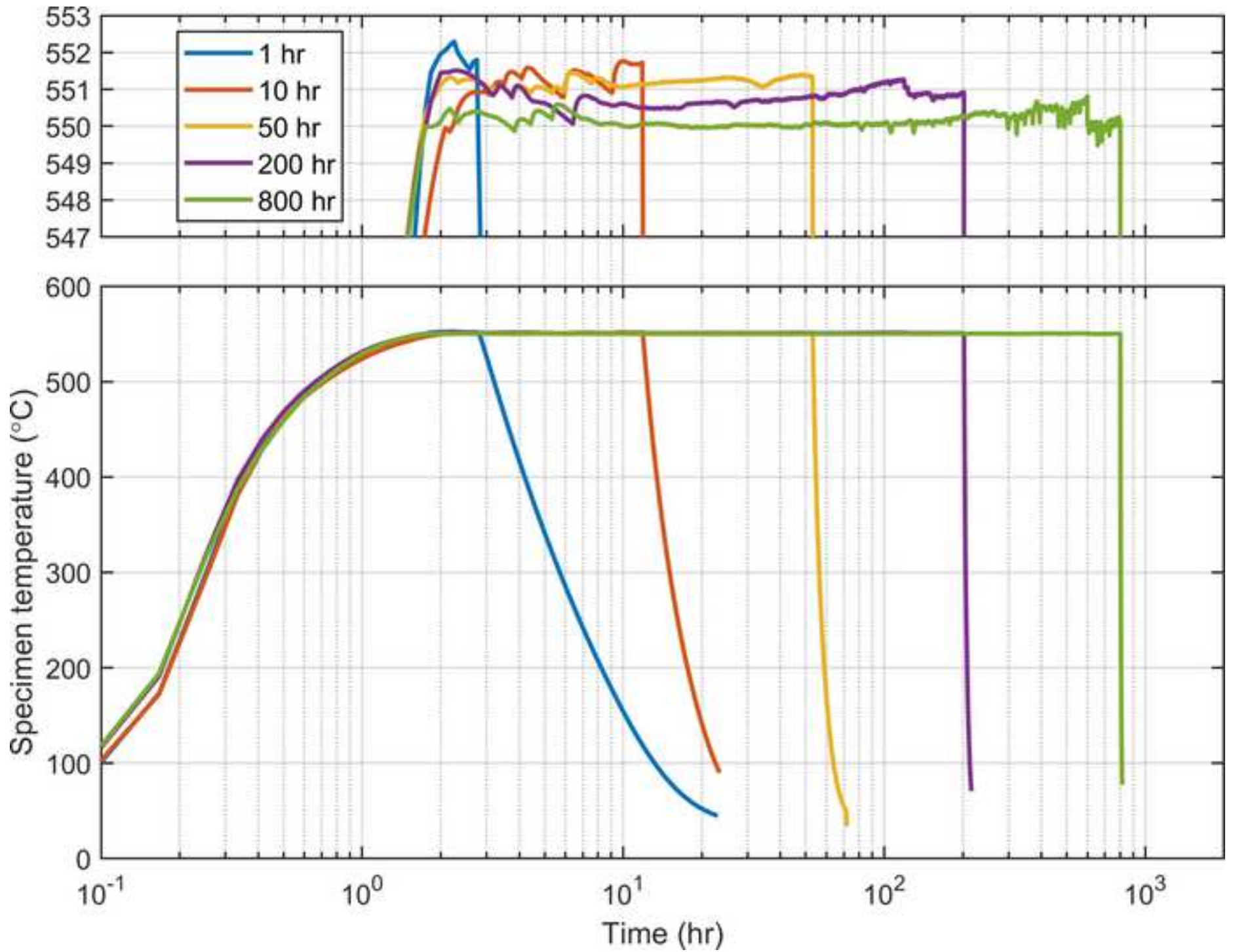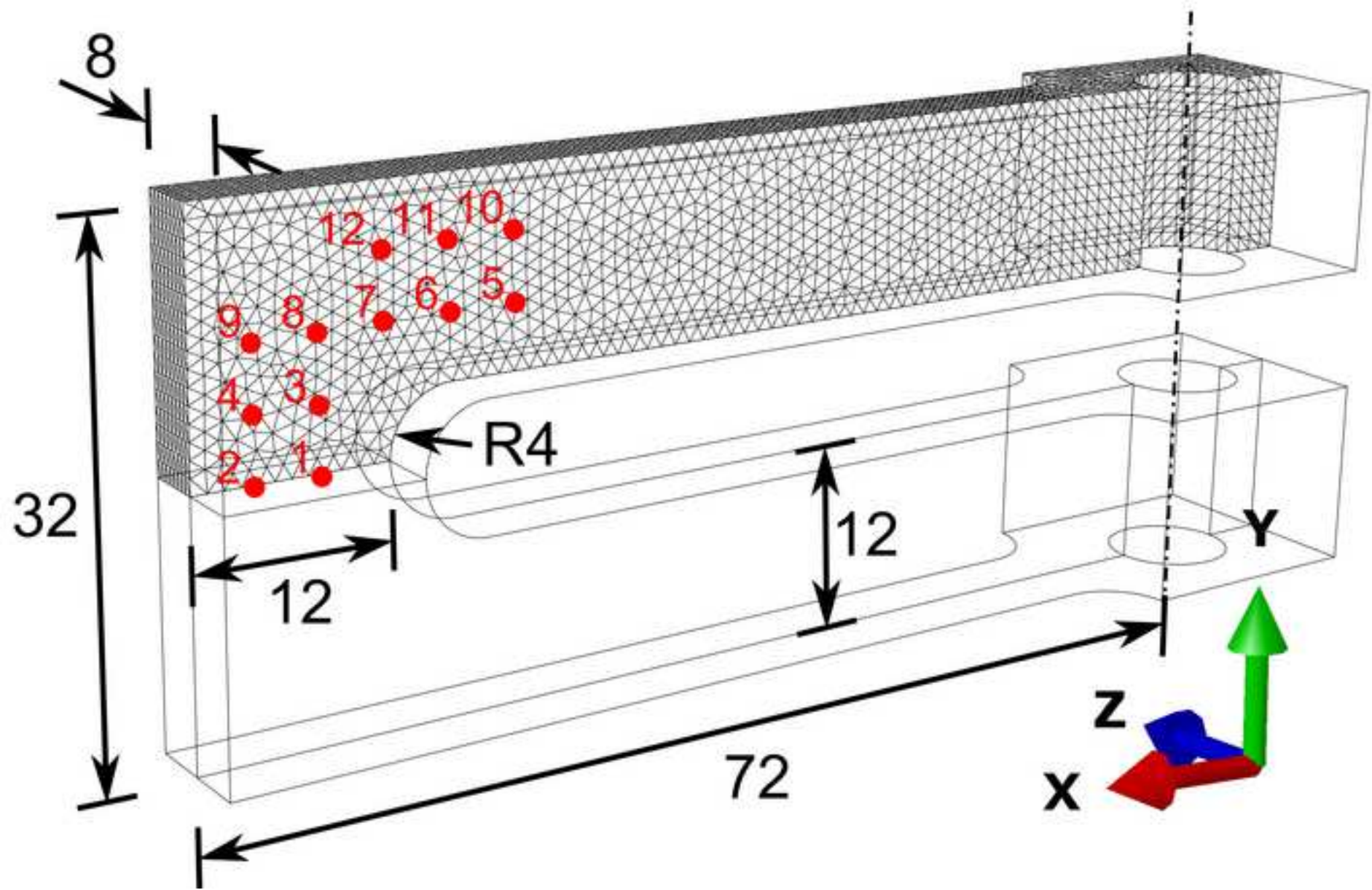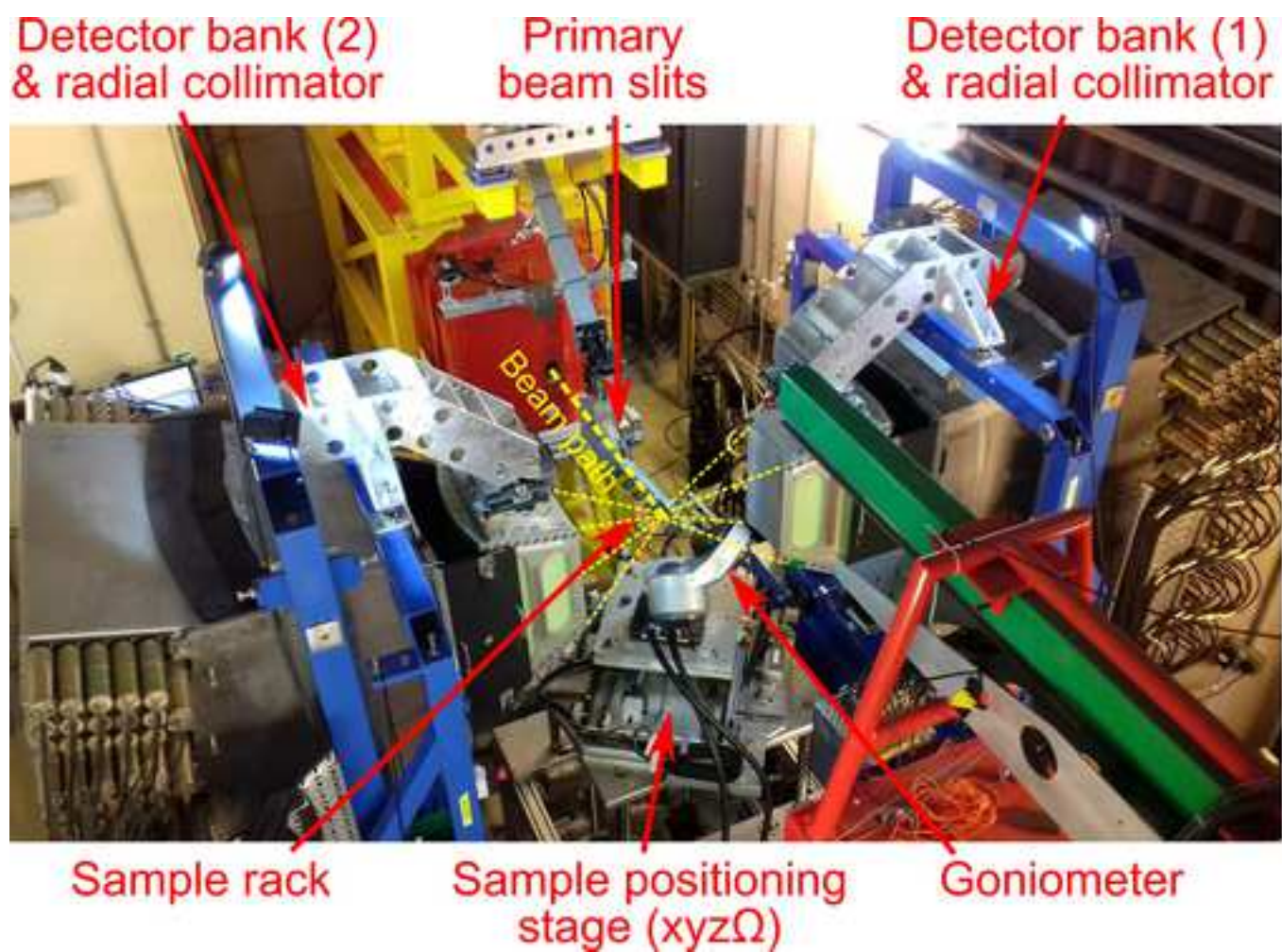
Figure 5
Click here to download high resolution image
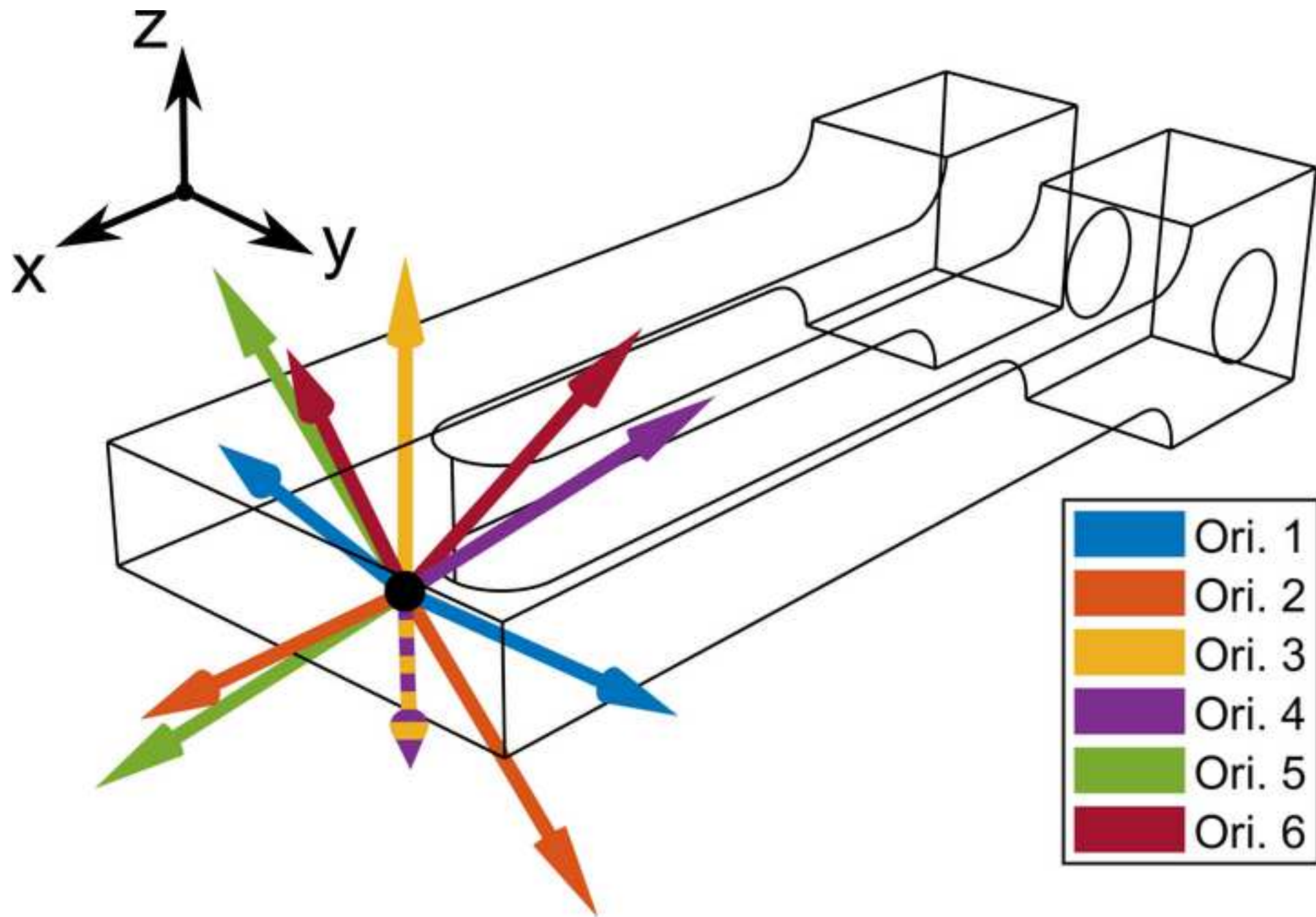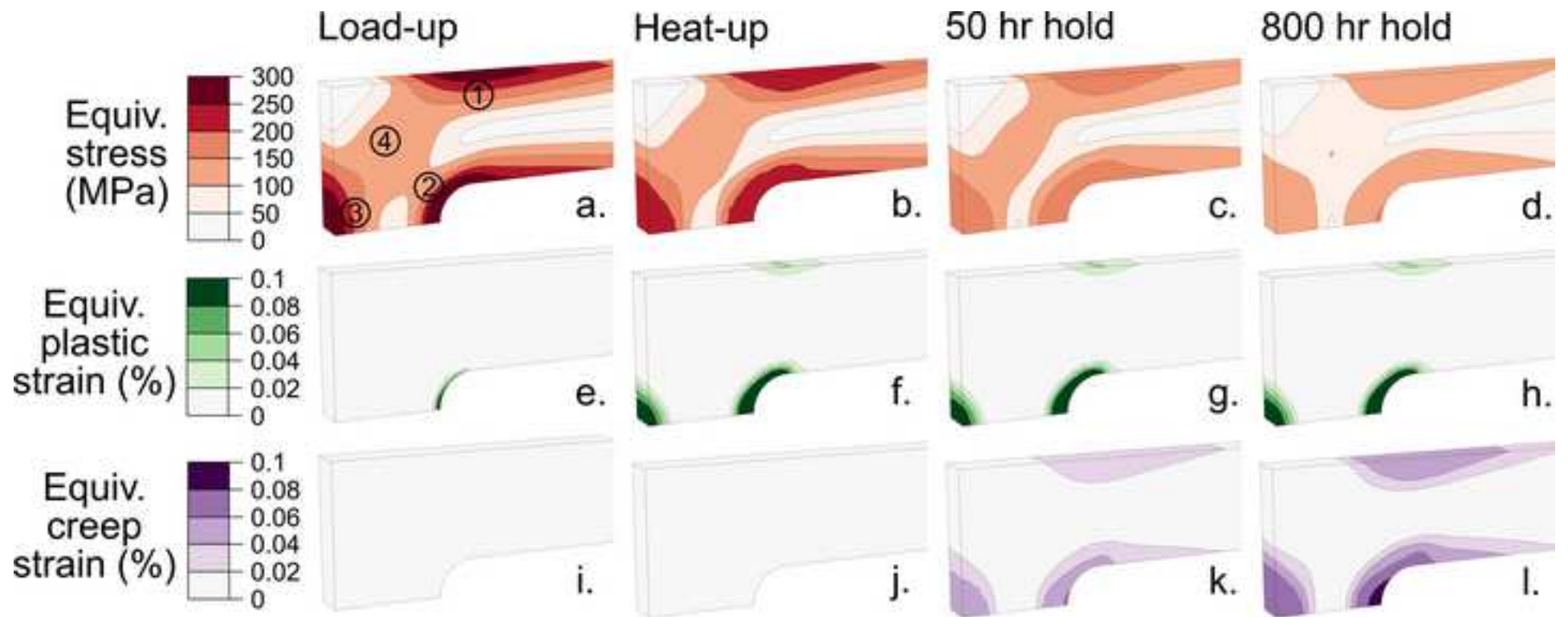
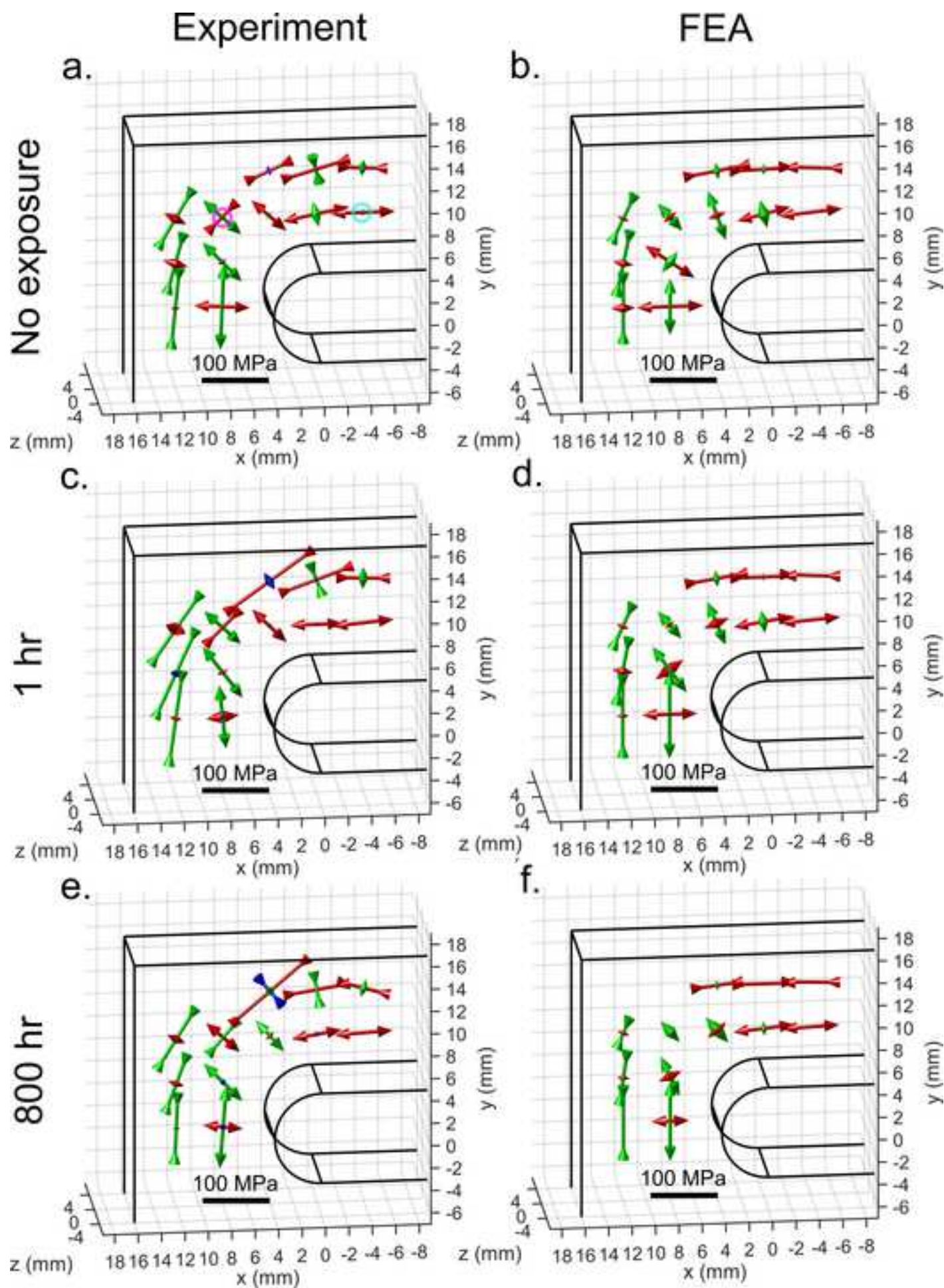**Figure 7**
[Click here to download high resolution image](#)
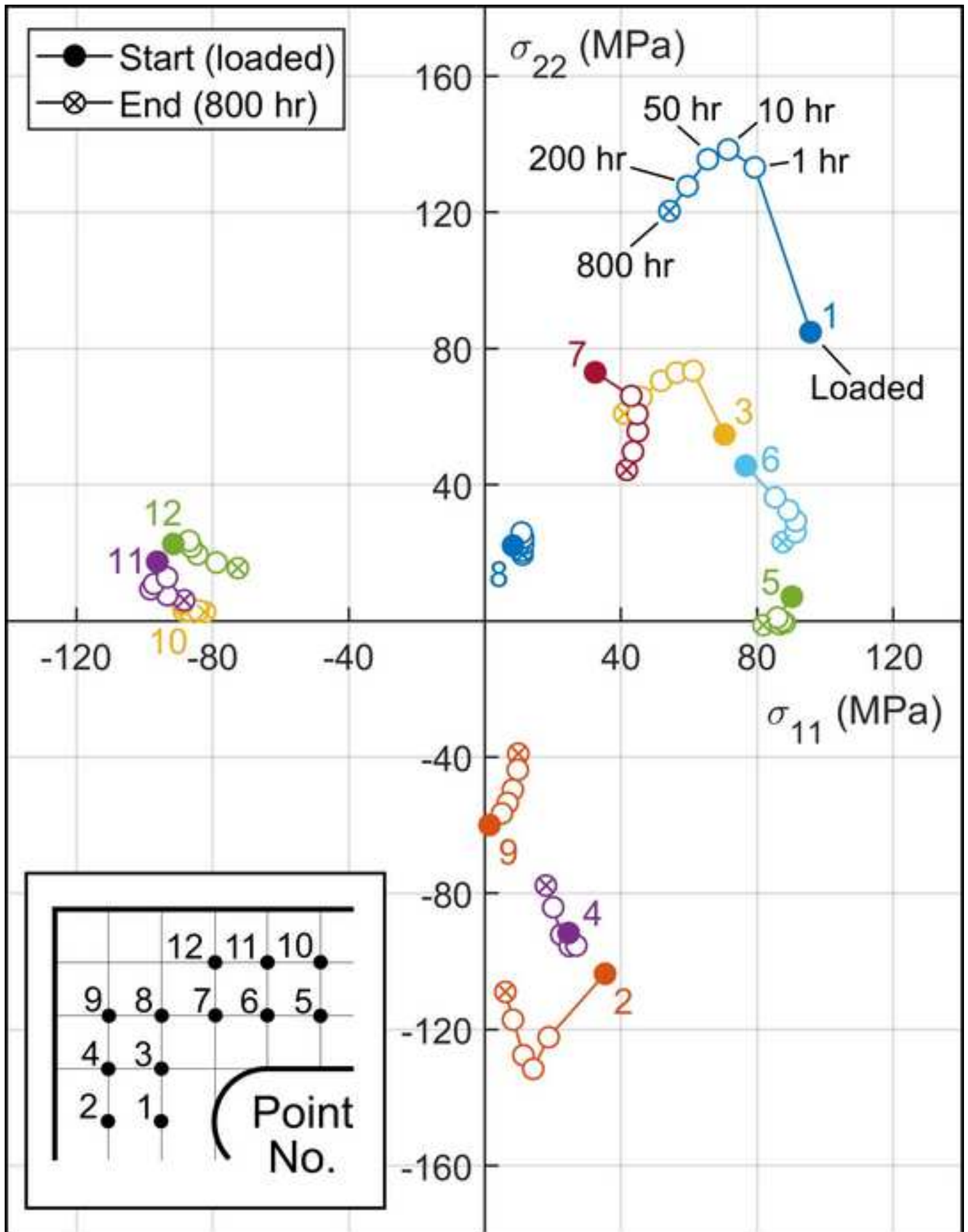
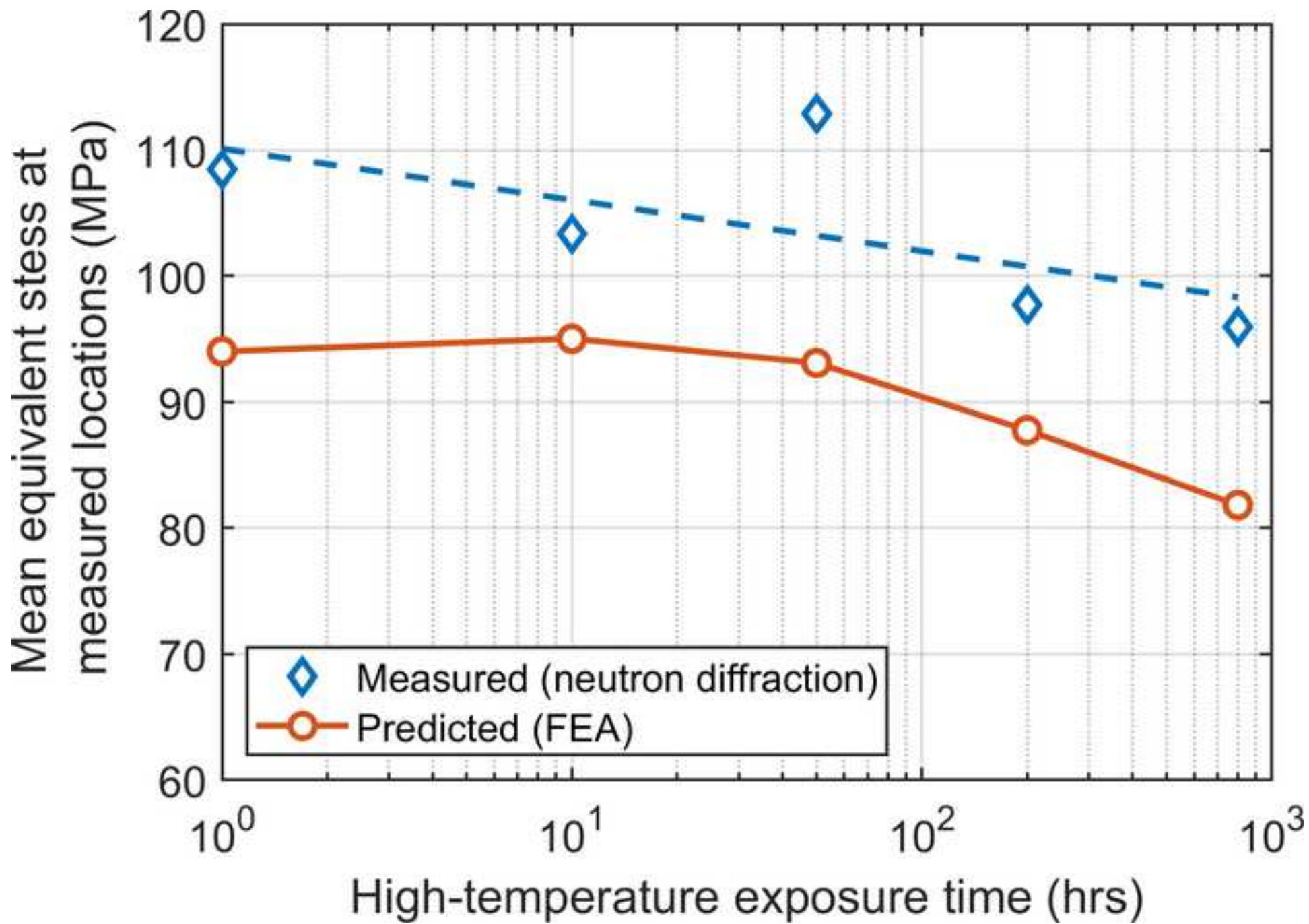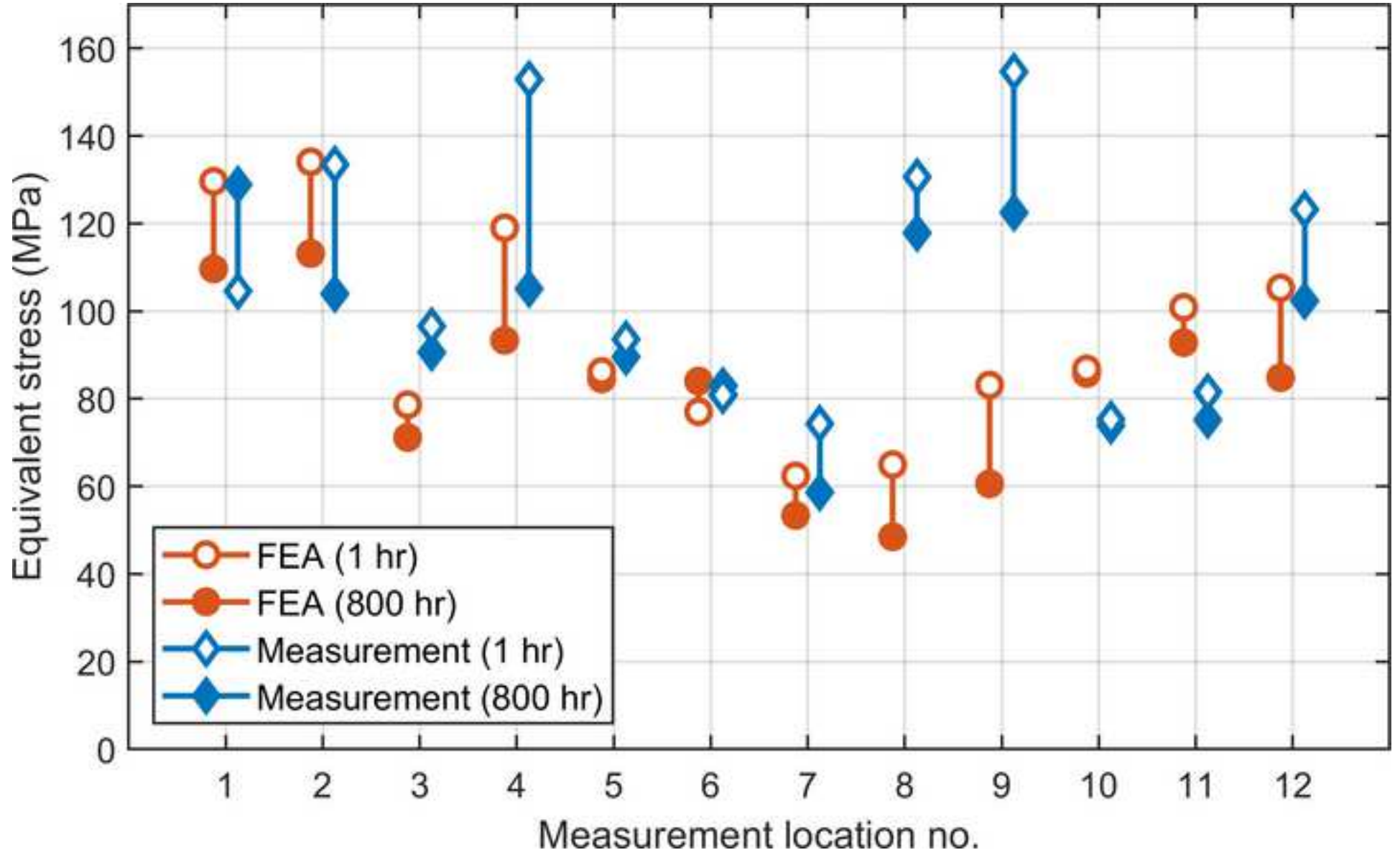**Figure 8**
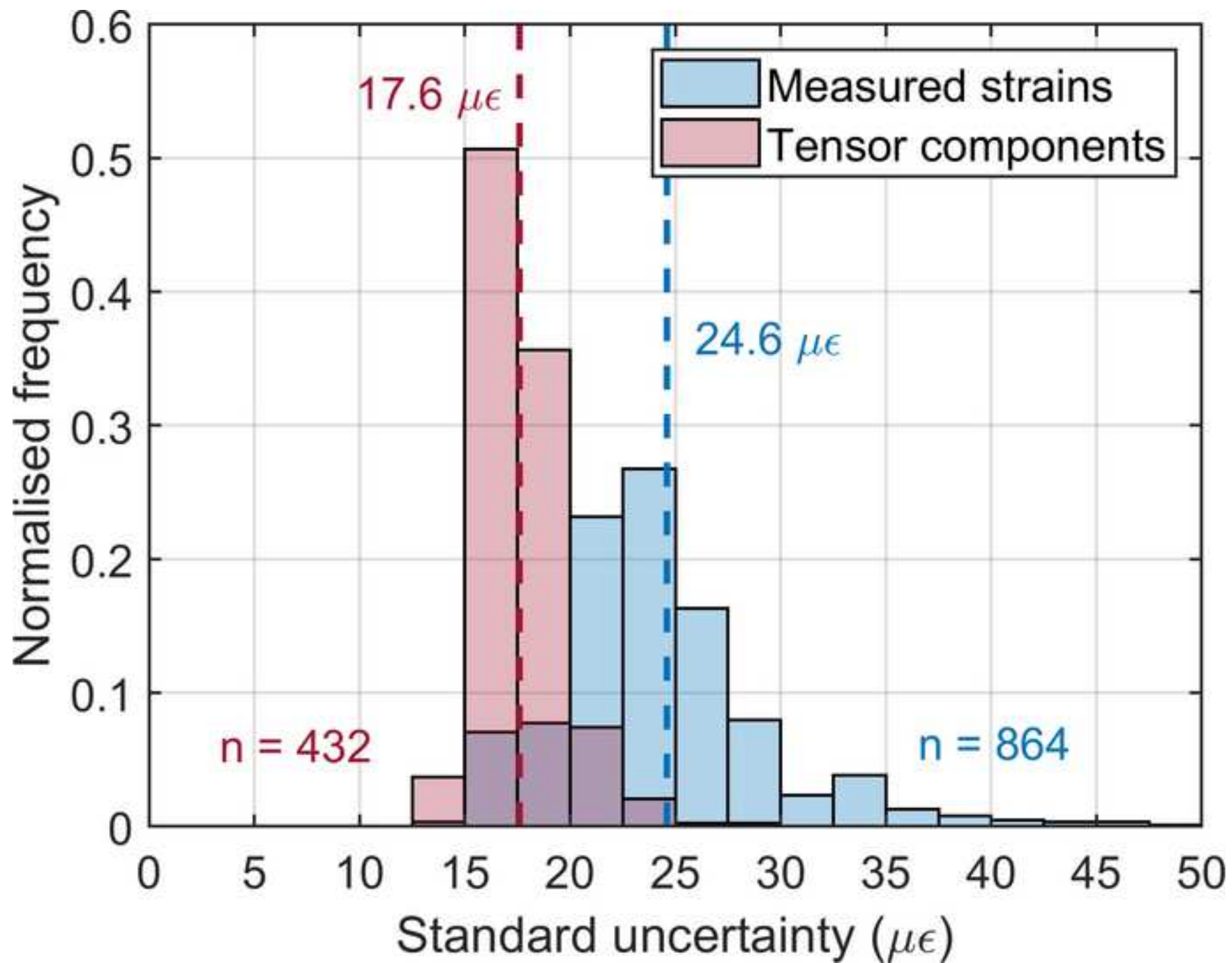**Click here to download high resolution image**

Credit Author Statement

Harry Coules: Conceptualisation, Investigation, Resources, Methodology, Funding acquisition, Writing – Original draft preparation, Visualisation.

Stephen Nneji: Investigation, Resources, Methodology

Jon James: Investigation, Resources, Methodology

Saurabh Kabra: Investigation, Methodology

Jianan Hu: Investigation, Resources, Writing – review & editing

Yiqiang Wang: Conceptualisation, Investigation, Resources, Writing – review & editing

*Highlights

- Neutron diffraction enables measurement of complete stress tensors inside homogeneous stainless steel specimens subject to high-temperature stress relaxation.
- Material deformation processes which cause a non-proportional change in multiaxial stress can be studied.
- Comparison with finite element analysis confirms that a widely-used creep rate law is conservative for multiaxial stressing.
- Reduction in stress tensor uncertainty is achievable using over-determined neutron diffraction measurements.

Declaration of interests

☒ The authors declare that they have no known competing financial interests or personal relationships that could have appeared to influence the work reported in this paper.

☐The authors declare the following financial interests/personal relationships which may be considered as potential competing interests: